

Two emitters coupled to a bath with Kerr-like nonlinearity: Exponential decay, fractional populations, and Rabi oscillations

J. Talukdar  and D. Blume 

Homer L. Dodge Department of Physics and Astronomy,

The University of Oklahoma, 440 West Brooks Street, Norman, Oklahoma 73019, USA

and Center for Quantum Research and Technology, The University of Oklahoma, 440 West Brooks Street, Norman, Oklahoma 73019, USA



(Received 3 March 2022; accepted 5 May 2022; published 2 June 2022)

We consider two noninteracting two-level emitters that are coupled weakly to a one-dimensional nonlinear waveguide. Due to the Kerr-like nonlinearity, the waveguide considered supports—in addition to the scattering continuum—a two-body bound state. As such, the waveguide models a bath with nontrivial mode structure. Solving the time-dependent Schrödinger equation, the radiation dynamics of the two emitters, initially prepared in their excited states, is presented. Changing the emitter frequency such that the two-emitter energy is in resonance with one of the two-body bound states, radiation dynamics ranging from exponential decay to fractional populations to Rabi oscillations is observed. Along with the detuning, the dependence on the separation of the two emitters is investigated. Approximate reduced Hilbert-space formulations, which result in effective emitter separation and momentum dependent interactions, elucidate the underlying physical mechanisms and provide an avenue to showcase the features that would be absent if the one-dimensional waveguide did not contain a nonlinearity. Our theoretical findings apply to a number of experimental platforms and the predictions can be tested with state-of-the-art technology. In addition, the weak-coupling Schrödinger equation based results provide critical guidance for the development of master equation approaches.

DOI: [10.1103/PhysRevA.105.063501](https://doi.org/10.1103/PhysRevA.105.063501)

I. INTRODUCTION

Since it is hard to fully isolate quantum systems in realistic experimental settings, the quantum-mechanical treatment of a system coupled to a bath is important from a practical point of view [1]. Taking a somewhat philosophical viewpoint, one may furthermore argue that truly isolated quantum systems never exist since any quantum system is part of a larger universe, i.e., embedded into an environment [2]. In addition, any measurement on the system involves, according to measurement theory, interactions between the system and the environment or bath [3–5].

The fact that systems are interacting with or can be made to interact with the environment that they are embedded into provides a wealth of opportunities. For example, bath engineering can be used to control the dynamics of the system, thereby providing an alternative approach to the preparation of prespecified target states [6–14]. The idea is quite simple. As an example, imagine two noninteracting few-level emitters that are both coupled to a bath. Even though the emitters are not interacting, the action of the bath on the emitters can be interpreted as an effective interaction between the emitters. The effective emitter-emitter interaction can be adjusted, by modifying the mode structure of the bath, such that the emitters are driven into a quasistationary state.

In most cases, the full quantum-mechanical treatment of the dynamics of the entire system, i.e., the system and the environment, is extremely challenging due to the tremendously large Hilbert space. To make progress, a range of

approaches has been pursued [15]. In the weak-coupling limit, perturbative and master equation approaches have been developed [16,17]. The strong-coupling limit can in some cases also be tackled perturbatively [18–24]. The present paper does not make any of these approximations and instead analyzes the dynamics of the emitter-waveguide system using the time-dependent Schrödinger equation, working—as, e.g., Refs. [25–31]—with the essentially full Hilbert space; the Hilbert-space truncation made (i.e., dropping of two-photon scattering states) leaves the dynamics essentially unchanged for the parameter combinations investigated. To make the calculations feasible, we restrict ourselves to a one-dimensional bath with a nontrivial but still relatively simple mode structure. Losses to the “outside world” are neglected entirely, i.e., the emitter-bath system is treated as a closed system (the waveguide is assumed to be lossless).

For concreteness, our paper focuses on a photonic lattice with lattice spacing a , nearest-neighbor tunneling J , and on-site interaction U [31,32]. The two two-level emitters are assumed to be located at or coupled to specific lattice sites [see Fig. 1(a)]. When both emitters are coupled to the same lattice site, the spacing x vanishes; when both emitters are coupled to adjacent lattice sites, x is equal to a ; and so on. This model Hamiltonian was introduced in Ref. [31]. While our paper builds on the theory framework introduced in Ref. [31], the emphasis of our paper is distinct. Specifically, our paper complements Ref. [31] in that we focus on the physics near the bottom or the top of the band as opposed to on the physics in the middle of the band, i.e., we consider a different range

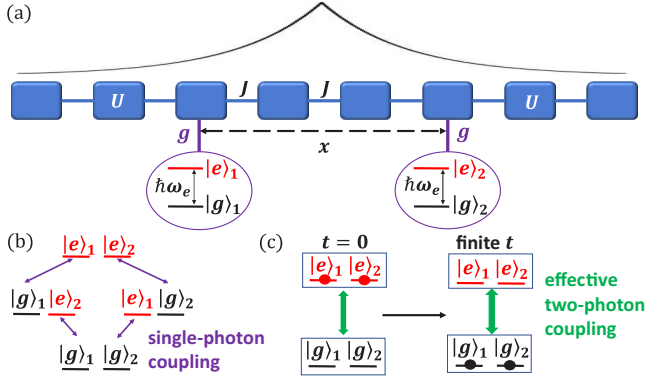


FIG. 1. Illustration of system under study. (a) Schematic of the system Hamiltonian. Each blue box represents a cavity. The tunnel coupling between neighboring cavities, which are separated by a , is shown by the lines labeled by J . The on-site interaction U characterizes the effective photon-photon interaction; the U term of the Hamiltonian \hat{H} , Eq. (2), only plays a role for $N_{\text{exc}} \geq 2$. Two two-level emitters with energy levels $|g\rangle_j$ and $|e\rangle_j$ ($j = 1$ or 2) are coupled to cavities n_1 and n_2 (n_1 and n_2 are fixed, $n_1 - n_2 = x/a$) with strength g . The black line illustrates a two-photon bound state that is supported by the cavity array. The physics explored in this paper occurs in the regime where the size of the two-photon bound state is comparable to the emitter separation x . (b) Illustration of the system-bath Hamiltonian \hat{H}_{sb} , Eq. (4), in the emitter Hilbert space. Going from $|e\rangle_1|e\rangle_2|\text{vac}\rangle$ to $|g\rangle_1|g\rangle_2|K\rangle$ requires two single-photon processes of strength g . (c) Illustration of the effective Hamiltonian \hat{H}^{adia} , Eq. (28), in the emitter Hilbert space. The adiabatic elimination introduces an effective two-photon coupling between states $|e\rangle_1|e\rangle_2|\text{vac}\rangle$ and $|g\rangle_1|g\rangle_2|K\rangle$. This paper monitors the change of the population of the state $|e\rangle_1|e\rangle_2|\text{vac}\rangle$ with time.

of detuning δ/J , where δ/J is defined with respect to the bottom of the two-photon bound-state band for negative U and with respect to the top of the two-photon bound-state band for positive U [33]:

$$\delta = 2\hbar\omega_e - 2\hbar\omega_c - \text{sgn}(U)\sqrt{U^2 + 16J^2}. \quad (1)$$

Here, $\hbar\omega_e$ is the transition energy of the emitter and $2\hbar\omega_c + \text{sgn}(U)\sqrt{U^2 + 16J^2}$ is the bottom of the band for negative U and the top of the band for positive U ($\hbar\omega_c$ is the energy in the middle of the single-photon energy band; see Fig. 2 for an illustration). We initialize the emitters in their excited state $|e\rangle_1|e\rangle_2$ and the waveguide in the vacuum state $|\text{vac}\rangle$ at time $t = 0$. Working in the subspace of two excitations, we study the radiation dynamics. Throughout, we refer to the bath as the photon bath. We emphasize, however, that the formalism applies also to a phonon bath and baths consisting of other quasiparticles. The Hamiltonian considered conserves the total number of excitations (see, e.g., Refs. [16,25,26,31,34]), which is defined as the sum of the number of emitter excitations and the number of photons. Key objectives of our paper are to unravel the dependence of the radiation dynamics on the emitter separation x and the detuning δ .

Our main results can be summarized as follows.

(i) The radiation dynamics depends strongly on the emitter separation, detuning, and strength of the nonlinearity.

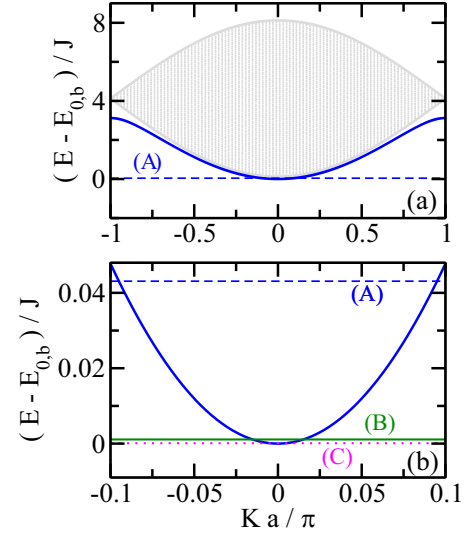


FIG. 2. Two-photon eigenspectrum as a function of the scaled center-of-mass wave number Ka/π . Note that the energy is shifted such that the bottom of the two-photon bound-state band sits at zero. (a) The gray-shaded energy band corresponds to the two-photon scattering continuum, Eq. (9). The thick blue solid line shows the energy $E_{K,b}$ of the two-photon bound state for $U/J = -1$. While the gray band and thick blue solid line appear to coincide for $K = 0$ on the scale shown, we note that the bottom of the two-photon scattering continuum at $K = 0$ lies $(-4 + \sqrt{17})J \approx 0.123J$ above the $K = 0$ two-photon bound-state energy. This separation is sufficiently large for the two-photon scattering continuum to play a negligible role in the system dynamics considered in this paper. The thin dashed line shows the energy of the state $|e, e, \text{vac}\rangle$ for $\delta/J = 0.0431$. (b) Blow-up of panel (a), focusing on the region around the bottom of the band. The blue solid and blue dashed lines are the same as in panel (a). The horizontal green solid and magenta dotted lines show the energy of the state $|e, e, \text{vac}\rangle$ for $\delta/J = 0.0011$ and 0.0001 , respectively. The labels “(A),” “(B),” and “(C)” refer to the three scenarios introduced in the second to last paragraph of Sec. II A.

(ii) Focusing on parameter combinations where the single-photon contributions can be eliminated adiabatically (this implies moderate x/a , not too large $|U|/J$, and detuning δ such that the system is on resonance with the two-photon band or just slightly off resonance), we observe radiation dynamics ranging from exponential decay to fractional population to Rabi oscillations.

(iii) As discussed in Ref. [31], the Markov approximation provides a faithful description of the exponential decay of the initial state; our semianalytic expression for the decay constant is compared with that for a single emitter case where the emitter energy is in resonance with the single-photon energy band, excluding the region near the bottom of the band.

(iv) When the on-site interaction is negative and the detuning is chosen such that the energy of the two emitters is in the band but close to the bottom of the band (the actual value of δ/J depends on the separation x and the coupling strength g/J), the emitters do not decay to the ground state but instead approach a steady state that is characterized by fractional populations. Some of the time-dependent characteristics can

be explained in terms of effective photon-pair–photon-pair interactions.

(v) Detuning extremely close to the bottom of the band [as in (iv)], the actual value of δ/J depends on the separation x and the coupling strength g/J leads to weakly damped or essentially undamped Rabi oscillations, which display a notable separation dependence and can be explained in terms of two bound hybridized photonic polaron–excited emitter states. An analytical two-state model that provides a semiquantitative description of the Rabi oscillations is derived.

We note in passing that our results in support of the conclusions summarized under (iii) form the basis for developing master equation formulations.

The remainder of this paper is organized as follows. Section II introduces the model Hamiltonian and the approaches used to solving the time-dependent and time-independent Schrödinger equation. Sections III and IV present our time-independent and time-dependent results. Last, Sec. V provides a summary and outlook. Appendix A reviews single-emitter results from the literature while Appendix B contains technical details related to the adiabatic elimination.

II. SYSTEM HAMILTONIAN AND THEORETICAL TECHNIQUES

Sections II A and II B introduce the full system Hamiltonian and the bath Hamiltonian, respectively. Our approach for solving the full Schrödinger equation is summarized in Sec. II C. The adiabatic elimination of the single-photon states is discussed in Sec. II D. Building on the reduced Hilbert-space Hamiltonian that results after the adiabatic elimination, Sec. II E discusses the Markov approximation.

A. System Hamiltonian

The total Hamiltonian \hat{H} is given by [31,32]

$$\hat{H} = \hat{H}_s + \hat{H}_b + \hat{H}_{sb}, \quad (2)$$

where \hat{H}_s denotes the system Hamiltonian, \hat{H}_b the bath Hamiltonian, and \hat{H}_{sb} the system-bath coupling [see Fig. 1(a) for a schematic]. We consider a system consisting of N_e two-level emitters with energy separation $\hbar\omega_e$ between the ground state $|g\rangle_j$ and the excited state $|e\rangle_j$ of the j th emitter. Specifically, \hat{H}_s is given by

$$\hat{H}_s = \frac{\hbar\omega_e}{2} \sum_{j=1}^{N_e} (\hat{\sigma}_j^z + \hat{I}_j), \quad (3)$$

where $\hat{\sigma}_j^z = |e\rangle_j\langle e| - |g\rangle_j\langle g|$ and $\hat{I}_j = |g\rangle_j\langle g| + |e\rangle_j\langle e|$. The inclusion of the identity $\sum_{j=1}^{N_e} \hat{I}_j$ in Eq. (3) introduces an energy shift such that the energy of the state with N_e emitters in their excited state and the bath in the vacuum state is equal to $N_e\hbar\omega_e$. The energy shift due to the identity introduces an overall phase in the time-dependent wave packet but does not impact the population dynamics. The j th emitter is coupled to the n_j th lattice site of the waveguide, i.e., the emitters do not move during the dynamics.

Triggered by the system-bath Hamiltonian \hat{H}_{sb} with coupling strength g , the emitters can change their state from $|e\rangle_j$

to $|g\rangle_j$ and from $|g\rangle_j$ to $|e\rangle_j$:

$$\hat{H}_{sb} = g \sum_{j=1}^{N_e} (\hat{a}_{n_j} \hat{\sigma}_j^+ + \hat{a}_{n_j}^\dagger \hat{\sigma}_j^-). \quad (4)$$

Here, $\hat{\sigma}_j^+$ and $\hat{\sigma}_j^-$ denote raising and lowering operators of the j th emitter, $\hat{\sigma}_j^+ = |e\rangle_j\langle g|$ and $\hat{\sigma}_j^- = |g\rangle_j\langle e|$. The operators $\hat{a}_{n_j}^\dagger$ and \hat{a}_{n_j} , respectively, create and destroy a photon at lattice site n_j , where the label n_j takes values from 1 to N with N denoting the number of lattice sites or cavities of the waveguide. We are interested in the regime where the dynamics is independent of N (large N limit). Since the system-bath Hamiltonian does not include any counter-rotating terms, the treatment is restricted to the weak-coupling regime where $|g|$ is small compared to the other energy scales of the system [35].

The Hamiltonian \hat{H}_b is taken to be a one-dimensional array of tunnel coupled cavities in the tight-binding limit. It is characterized by the “photon energy” $\hbar\omega_c$ (the middle of the single-photon energy band has energy $\hbar\omega_c$), the tunneling energy J , and the on-site interaction energy U :

$$\begin{aligned} \hat{H}_b = & \hbar\omega_c \sum_{n=1}^N \hat{a}_n^\dagger \hat{a}_n - J \sum_{n=1}^N (\hat{a}_n^\dagger \hat{a}_{n+1} + \hat{a}_{n+1}^\dagger \hat{a}_n) \\ & + \frac{U}{2} \sum_{n=1}^N \hat{a}_n^\dagger \hat{a}_n^\dagger \hat{a}_n \hat{a}_n. \end{aligned} \quad (5)$$

In Eq. (5), the photons are assumed to interact, due to the presence of a Kerr-like medium, either effectively repulsively ($U > 0$) or effectively attractively ($U < 0$). A positive U gives rise to a two-photon bound state with center-of-mass wave vector K that lies above the two-photon continuum while a negative U gives rise to a two-photon bound state with center-of-mass wave vector K that lies below the two-photon scattering continuum [36–39].

The bath Hamiltonian considered here has been chosen for several reasons.

(i) The eigenenergies and eigenstates of \hat{H}_b are known analytically (see below) [38].

(ii) Despite its simplicity, the Hamiltonian \hat{H}_b supports a nontrivial mode structure, namely, the above-mentioned two-photon bound state [36–39].

(iii) It was predicted in Ref. [31] that the emission dynamics of \hat{H} displays, for certain parameter combinations, subradiance and supercorrelations.

These intriguing findings motivate our quest to map out constructive and destructive interferences, with the goal of identifying the dominant emission pathways. Throughout, we are interested in situations where the initial $t = 0$ state contains two excitations in the emitter Hilbert space (i.e., $|\Psi(0)\rangle = |e\rangle_1|e\rangle_2|\text{vac}\rangle$) and where the dynamics is driven, at least in part, by the nontrivial mode structure of the bath, i.e., by the existence of the two-photon bound states supported by \hat{H}_b . For brevity, we adopt the notation $|e\rangle_1|e\rangle_2|\text{vac}\rangle = |e, e, \text{vac}\rangle$, etc. The next section discusses selected properties of \hat{H}_b .

The Hamiltonian \hat{H} has four independent energy scales: δ , g , J , and U . Throughout, J , \hbar/J , and a are used as energy

unit, time unit, and length unit, respectively. To reduce the parameter space, we analyze the system properties for fixed g/J as functions of δ/J and x/a . The dependence on U/J is explored a bit; most calculations presented, however, are for $U/J = -1$. Throughout, we work in the weak-coupling regime, i.e., we use $g/J = 1/50$. Section V comments briefly on the dependence of the system properties on g/J . As illustrated in Fig. 2, the detuning δ is set such that the energy $2\hbar\omega_e$ of the initial state is, for $g = 0$, (A) in resonance with a two-photon bound state with Ka/π not too close to zero and not too close to ± 1 [see the horizontal dashed line in Fig. 2(b) as an example]; (B) in resonance with a two-photon bound state with Ka/π a bit larger than zero [see the horizontal solid line in Fig. 2(b) as an example]; and (C) in resonance with the two-photon bound state extremely close to the bottom of the band [$K^{(0)}a/\pi \approx 4.5 \times 10^{-3}$; see the horizontal dotted line in Fig. 2(b) as an example].

We note that single-photon losses are not included in our treatment. This is justified if the dynamics governed by \hat{H} is notably faster than the dynamics associated with the single-photon losses. Using the parameters of Fig. 11 as an example, this implies that the single-photon loss rate is assumed to be smaller than $\approx 10^{-4}J/\hbar$.

B. Mode structure of the bath Hamiltonian

Since the Hamiltonian \hat{H}_b commutes with the photon number operator \hat{N} [36–38],

$$\hat{N} = \sum_{n=1}^N \hat{a}_n^\dagger \hat{a}_n, \quad (6)$$

\hat{H}_b is block diagonal in the number of photons. In what follows, we discuss the eigenspectrum of \hat{H}_b in the one- and two-photon subspaces.

We start with the single-photon subspace. The single-photon energy E_k reads [40]

$$E_k = \hbar\omega_c - 2J \cos(ka), \quad (7)$$

where the single-photon wave number k ($ka/\pi \in [-1, 1]$) is a good quantum number. The single-photon eigenstates with energy E_k are denoted by $|\psi_k\rangle$. Equation (7) shows that E_k is equal to $\hbar\omega_c$ for $ka/\pi = \pm 1/2$ (this is the middle of the band), equal to $\hbar\omega_c - 2J$ for $ka/\pi = 0$ (this is the bottom of the band), and equal to $\hbar\omega_c + 2J$ for $ka/\pi = \pm 1$. For later reference, we note that the single-photon group velocity v_k is given by

$$v_k = \frac{2Ja}{\hbar} \sin(ka). \quad (8)$$

This shows that a single photon travels, “on average,” two lattice sites per characteristic time \hbar/J for $ka/\pi = \pm 1/2$ and not at all for $ka = 0$ and $ka/\pi = \pm 1$. According to this classical average-speed-picture, two individually launched photons may not interfere with each other if the photon’s wave number is close to zero or $\pm\pi/a$, or if the emitters are separated by many lattice sites.

We now turn to the two-photon subspace, which is spanned by scattering states $|\psi_{K,q}\rangle$ with energy $E_{K,q}$ and bound states $|\psi_{K,b}\rangle$ with energy $E_{K,b}$ [36–39]. The center-of-mass

wave number K is a good quantum number. The gray band in Fig. 2(a) shows the two-photon scattering energy $E_{K,q}$ [36–38],

$$E_{K,q} = 2\hbar\omega_c - 4J \cos\left(\frac{Ka}{2}\right) \cos(qa), \quad (9)$$

as a function of K ($Ka/\pi \in [-1, 1]$). The energy continuum arises from the fact that the relative wave number q can take a range of values that depends on K (e.g., $qa/\pi \in [-1, 1]$ for $K = 0$ and $qa/\pi = 0$ for $Ka/\pi = \pm 1$). The middle of the scattering continuum lies at $2\hbar\omega_c$, and the scattering continuum has a width of $8J$ for $Ka/\pi = 0$ and a width of zero for $Ka/\pi = \pm 1$. While the two-photon scattering energies $E_{K,q}$ are independent of U , the associated scattering states depend on U .

In addition, the Hamiltonian \hat{H}_b supports one two-photon bound state with energy $E_{K,b}$ for each K [36–39]:

$$E_{K,b} = 2\hbar\omega_c + \text{sign}(U) \left[U^2 + 16J^2 \cos^2\left(\frac{Ka}{2}\right) \right]^{1/2}. \quad (10)$$

For negative U/J , the bound state lies below the scattering continuum (see the thick blue solid line in Fig. 2 for $U/J = -1$). In this case, the binding energy for a given K is defined as the energy difference between the lower edge of the scattering continuum ($E_{K,q}$ with $q = 0$) and the bound-state energy $E_{K,b}$. The situation for positive U/J is similar, except that the bound state lies above the scattering continuum. The binding energy increases with increasing $|U|/J$; correspondingly, the two-photon bound-state wave function becomes more localized. We note that two-photon bound states [41] and repulsively bound atom pairs in optical lattices [42] have been observed experimentally.

The horizontal lines in Fig. 2(b) show the energy of the state $|e\rangle_1 |e\rangle_2 |\text{vac}\rangle$ for three different values of δ/J : $\delta/J = 0.0431$ (dashed line) corresponds to scenario A, $\delta/J = 0.0011$ (solid line) corresponds to scenario B, and $\delta/J = 0.0001$ (dotted line) corresponds to scenario C. The crossings between the energy of the initial state and the energy $E_{K,b}$ of the two-photon bound state define the uncoupled (i.e., $g = 0$) resonance wave numbers $\pm K^{(0)}$ [31], where $K^{(0)}$ is defined to be positive. For finite coupling strength g , the value of the resonance wave vector shifts from $K^{(0)}$ to $K^{(*)}$ (see Appendix B for details).

In scenario A, radiation is emitted predominantly, via intermediate single-photon states, into two-photon bound states with wave numbers $\approx \pm K^{(*)}$, leading to exponential decay [31]. Since the group velocity $v_{K,b}$ [38],

$$v_{K,b} = \frac{1}{\hbar} \frac{\partial E_{K,b}}{\partial K}, \quad (11)$$

of the two-photon bound state depends on K ($v_{K,b}$ is zero for $Ka/\pi = 0$ and ± 1 and finite for all other Ka), the decay constant shows a distinct dependence on the resonance wave number or, equivalently, on the detuning δ/J [31]. In scenario B, the near flatness of the band implies that the initial energy is nearly equal to that of several two-photon bound states with $|Ka/\pi| \ll 1$. This leads, as shown in Sec. IV, to fractional populations. In scenario C, the two-photon bound-state band splits into a band and an emitter-photon coupling induced polaronlike bound state that hybridizes with the state $|e, e, \text{vac}\rangle$

upon inclusion of the coupling between the polaronlike bound state and the state $|e, e, \text{vac}\rangle$, leading to essentially undamped Rabi oscillations that are reproduced very well by a two-state model. Selected results for scenarios B and C are discussed in Ref. [32].

C. Solving the Schrödinger equation

Since \hat{H} commutes with the excitation operator \hat{N}_{exc} [16,25,26,31,34],

$$\hat{N}_{\text{exc}} = \hat{N} + \sum_{j=1}^{N_e} \hat{\sigma}_j^+ \hat{\sigma}_j^-, \quad (12)$$

the number of excitations N_{exc} (eigenvalue of \hat{N}_{exc}) is conserved. Correspondingly, the time evolution of an initial state with $N_{\text{exc}} = 2$ under the Hamiltonian \hat{H} , Eq. (2), can be expanded in terms of the states $|e, e, \text{vac}\rangle$, $\hat{a}_n^\dagger |e, g, \text{vac}\rangle$, $\hat{a}_n^\dagger |g, e, \text{vac}\rangle$, and $\hat{a}_n^\dagger \hat{a}_{n'}^\dagger |g, g, \text{vac}\rangle$, where n and n' take the values $1, \dots, N$. Alternatively, the time-dependent state $|\Psi(t)\rangle$ can be expanded using the zero-, one-, and two-photon eigenstates of \hat{H}_b [31]:

$$|\Psi(t)\rangle = \exp(-2i\omega_e t) [c_{ee}(t) |e, e, \text{vac}\rangle + \sum_k c_{1k}(t) \hat{a}_k^\dagger |e, g, \text{vac}\rangle]$$

$$i\hbar \dot{c}_{\alpha k}(t) = \Delta_k c_{\alpha k}(t) + \frac{g}{\sqrt{N}} \exp(-i k a n \beta) c_{ee}(t) + \frac{g}{N} \sum_K M_b(k, n_\alpha, K) c_{K,b}(t) + \frac{g}{N} \sum_{K,q} M_q(k, n_\alpha, K) c_{K,q}(t), \quad (17)$$

$$i\hbar \dot{c}_{K,b}(t) = \Delta_{K,b} c_{K,b}(t) + \frac{g}{N} \sum_{\alpha=1,2} \sum_k [M_b(k, n_\alpha, K)]^* c_{\alpha k}(t), \quad (18)$$

and

$$i\hbar \dot{c}_{K,q}(t) = \Delta_{K,q} c_{K,q}(t) + \frac{g}{N} \sum_{\alpha=1,2} \sum_k [M_q(k, n_\alpha, K)]^* c_{\alpha k}(t). \quad (19)$$

For $N_{\text{exc}} = 2$ (recall, this is the focus of our paper), Eqs. (16)–(19) are equivalent to the time-dependent Schrödinger equation. The quantities Δ_k , $\Delta_{K,b}$, and $\Delta_{K,q}$ denote energy detunings:

$$\Delta_k = E_k - \hbar\omega_e, \quad (20)$$

$$\Delta_{K,b} = E_{K,b} - 2\hbar\omega_e, \quad (21)$$

and

$$\Delta_{K,q} = E_{K,q} - 2\hbar\omega_e. \quad (22)$$

In Eq. (17), α takes the value 1 or 2. The value of β depends on α : $\beta = 2$ for $\alpha = 1$ and $\beta = 1$ for $\alpha = 2$ in Eqs. (16) and (17). The matrix elements $M_b(k, n, K)$ and $M_q(k, n, K)$ measure the contribution of a photon with wave number k to the two-photon bound state and to the two-photon scattering state, respectively, after acting with \hat{a}_n on the two-photon state:

$$M_b(k, n, K) = N \langle \psi_k | \hat{a}_n | \psi_{K,b} \rangle \quad (23)$$

$$+ \sum_k c_{2k}(t) \hat{a}_k^\dagger |g, e, \text{vac}\rangle + \sum_K c_{K,b}(t) \hat{P}_{K,b}^\dagger |g, g, \text{vac}\rangle + \sum_{K,q} c_{K,q}(t) \hat{P}_{K,q}^\dagger |g, g, \text{vac}\rangle], \quad (13)$$

where $|\psi_k\rangle = \hat{a}_k^\dagger |\text{vac}\rangle$, $|\psi_{K,b}\rangle = \hat{P}_{K,b}^\dagger |\text{vac}\rangle$, and $|\psi_{K,q}\rangle = \hat{P}_{K,q}^\dagger |\text{vac}\rangle$. The operators \hat{a}_n^\dagger and \hat{a}_k^\dagger are related via a Fourier transform in the standard way:

$$\hat{a}_k^\dagger = \frac{1}{\sqrt{N}} \sum_{n=1}^N \exp(i k a n) \hat{a}_n^\dagger. \quad (14)$$

Inserting Eq. (13) into the time-dependent Schrödinger equation

$$i\hbar \frac{\partial \Psi(t)}{\partial t} = \hat{H} \Psi(t) \quad (15)$$

and projecting onto the basis states, we obtain a set of first-order differential equations for the time-dependent expansion coefficients [31]:

$$i\hbar \dot{c}_{ee}(t) = \frac{g}{\sqrt{N}} \sum_{\alpha=1,2} \sum_k \exp(i k a n \beta) c_{\alpha k}(t), \quad (16)$$

and

$$M_q(k, n, K) = N \langle \psi_k | \hat{a}_n | \psi_{K,q} \rangle. \quad (24)$$

The matrix element $M_b(k, n, K)$ reads [31]

$$M_b(k, n, K) = \sqrt{2} \sum_m \exp \left[i m \left(k - \frac{K}{2} \right) a + i n (K - k) a \right] \psi_{K,b}(m), \quad (25)$$

where $\psi_{K,b}(m) = \langle r = ma | \psi_{K,b} \rangle$ with $|r\rangle$ denoting the relative distance between the two photons; $M_q(k, n, K)$ is obtained by replacing the subscript b in Eq. (25) by q . The matrix elements $M_b(k, n, K)$ and $M_q(k, n, K)$ are defined such that their values for a given k, n , and K [and q for $M_q(k, n, K)$] are independent of N ; they differ by a factor N from those defined in Ref. [31].

We solve the coupled differential equations by discretizing the wave numbers k, K , and q . For N lattice sites and $N_{\text{exc}} = 2$ excitations, we have $N^2 + (N_e + 1)N + 1$ expansion coefficients. If the scattering continuum can be neglected,

the computational complexity reduces dramatically since the number of coupled equations reduces from order N^2 to order N . For the parameters considered in this paper, we found—by performing calculations for $N \leq 300$ —that the scattering continuum plays a negligible role. This is consistent with the findings of Ref. [31]. Thus, the results presented are calculated using N up to 9001, excluding the scattering continuum from the Hilbert space.

Two numerical approaches are used. First, we use the Runge-Kutta algorithm [43] with adjustable time step to propagate the coefficients for a given initial state at $t = 0$ to time t . Second, we express the Hamiltonian \hat{H} in terms of the uncoupled $g = 0$ basis states using the matrix elements defined above. Determining the finite g eigenstates through diagonalization, we project the initial state onto the eigenstates of \hat{H} . Since the exact diagonalization approach is numerically more stable, the results presented in this paper are obtained using that approach.

The eigenspectrum of \hat{H} provides complementary clues for understanding the emitter dynamics. For finite g , eigenstates with hybridized character that contain photon and emitter contributions can exist [32]; for certain parameter combinations, these strongly mixed states have energies that lie “outside” the two-photon bound-state band. These states are discussed in more detail in Sec. III. Hybridized light-matter states play a critical role in many other related contexts [44–47].

D. Adiabatic elimination of single-photon states

This section discusses the construction of a reduced dimensionality Hamiltonian that “lives” in the Hilbert space spanned by the states $|g, g, \text{vac}\rangle$, $\hat{P}_{K,b}^\dagger |g, g, \text{vac}\rangle$, and $\hat{P}_{K,q}^\dagger |g, g, \text{vac}\rangle$. The basis states $\hat{a}_k^\dagger |e, g, \text{vac}\rangle$ and $\hat{a}_k^\dagger |g, e, \text{vac}\rangle$ are removed and accounted for approximately through effective interactions in the reduced dimensionality Hilbert space [see Figs. 1(b) and 1(c)]. The construction of the reduced dimensionality

Hamiltonian is based on the adiabatic elimination of $c_{1k}(t)$ and $c_{2k}(t)$ from the coupled equations [31,48]. The approximation requires that the change of $c_{1k}(t)$ and $c_{2k}(t)$ with time in Eqs. (16)–(19) can be neglected.

Even though the adiabatic elimination approach removes $c_{1k}(t)$ and $c_{2k}(t)$ from the coupled equations, we emphasize that the single-photon states play an important role even in the regime where the differential equations after adiabatic elimination provide a faithful description of the dynamics. This can be seen by inspecting Eqs. (16)–(19). If we start, e.g., with $c_{ee}(0) = 1$, then the evolution of the initial state for $t = 0^+$ is driven by the change of $\dot{c}_{\alpha k}(t)$; this follows since the $c_{ee}(t)$ coefficient appears on the right-hand side of Eq. (17) but not on the right-hand side of Eqs. (18) and (19). The key point of the adiabatic elimination is that the single-photon states serve as intermediate states—population goes into and out of these states at roughly equal rates such that the majority of the population is in the basis states with two emitter excitations and zero emitter excitations. The adiabatic elimination breaks down when g becomes too large (the actual value of g/J depends on the values of δ/J , U/J , and x/a).

Carrying out the adiabatic elimination and neglecting the effective coupling matrix elements $H_{K,K',q}(n_1, n_2)$ and $J_{K,K',q,q}(n_1, n_2)$ that involve the two-photon scattering continuum (see Appendix B), Eqs. (16)–(19) reduce to a set of differential equations that can be written in terms of the effective adiabatic Hamiltonian \hat{H}^{adia} . In matrix form, we find [31]

$$i\hbar \frac{\partial}{\partial t} \begin{pmatrix} c_{ee}(t) \\ \vec{c}_{K,b}(t) \end{pmatrix} = \underline{H}^{\text{adia}} \begin{pmatrix} c_{ee}(t) \\ \vec{c}_{K,b}(t) \end{pmatrix}, \quad (26)$$

where

$$\vec{c}_{K,b}(t) = (c_{K_1,b}(t), \dots, c_{K_N,b}(t))^T, \quad (27)$$

$$\underline{H}^{\text{adia}} = \begin{pmatrix} 2\Delta_e & 0 \\ 0 & \underline{\Delta}_{K,b} \end{pmatrix} + \frac{g^2}{J} \begin{pmatrix} 0 & N^{-1/2}(\vec{F}_{K,b}(n_1, n_2))^T \\ N^{-1/2}[\vec{F}_{K,b}(n_1, n_2)]^* & N^{-1}\underline{G}_{K,K'}(n_1, n_2) \end{pmatrix}, \quad (28)$$

and

$$\vec{F}_{K,b}(n_1, n_2) = (F_{K_1,b}(n_1, n_2), \dots, F_{K_N,b}(n_1, n_2))^T. \quad (29)$$

The definition of the vector $\vec{F}_{K,b}(n_1, n_2)$ is given in Eq. (B4). The matrices $\underline{\Delta}_{K,b}$ and $\underline{G}_{K,K'}(n_1, n_2)$ have dimension $N \times N$: $\underline{\Delta}_{K,b}$ is diagonal with $\Delta_{K_1,b}, \dots, \Delta_{K_N,b}$ on the diagonal and the elements of $\underline{G}_{K,K'}(n_1, n_2)$ are given by $G_{K_l, K_{l'}}(n_1, n_2)$ [Eq. (B6)], with l and l' taking the values $1, \dots, N$. The second term on the right-hand side of Eq. (28) represents effective interactions that arise due to the elimination of the single-photon states. The element $F_{K_l,b}(n_1, n_2)$ represents an effective interaction between the state $|e, e, \text{vac}\rangle$ and the two-photon bound state with center-of-mass wave number K_l while the element $G_{K_l, K_{l'}}(n_1, n_2)$ represents an effective interaction between the two-photon bound state with wave number K_l and the two-photon bound state with wave number $K_{l'}$. We note

that $F_{K_l}(n_1, n_2)$ and $G_{K_l, K_{l'}}(n_1, n_2)$ are independent of g and, in general, complex.

Figure 3 shows $\vec{F}_{K,b}(n_1, n_2)$ as functions of Ka/π and x/a for $\delta/J = 0.0011$ and two different U/J , namely, $U/J = -1$ (top row) and $U/J = -5/2$ (bottom row). The real and imaginary parts of $\vec{F}_{K,b}(n_1, n_2)$ are shown in the left and right columns, respectively. We note that the system properties only depend on the emitter separation x/a and not independently on the actual emitter positions n_1 and n_2 ; to make Fig. 3, the separation is—to aid with the visualization—treated as a continuous as opposed to a discrete variable. The magnitude of the real part of the effective interactions is larger for $U/J = -1$ (weakly bound state) than for $U/J = -5/2$ (more strongly bound state). The characteristics common to both U/J values considered in Fig. 3 are as follows: First, the real part of the effective interactions is most negative near $Ka/\pi = x/a = 0$, even though the resonance wave vector $K^{(0)}$ differs in the

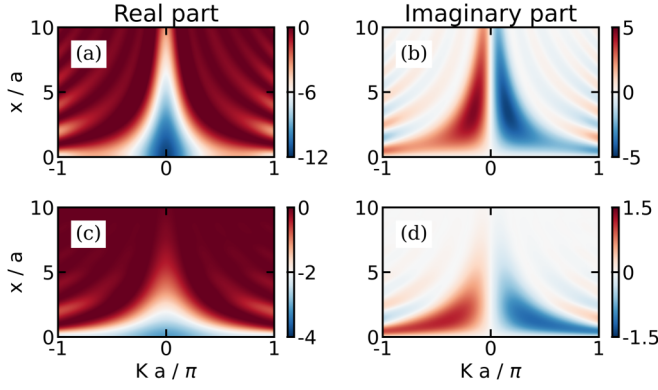


FIG. 3. Contour plots of the effective dimensionless interactions $\vec{F}_{K,b}(n_1, n_2)$ between the states $|e, e, \text{vac}\rangle$ and $\hat{P}_{K,b}^\dagger|g, g, \text{vac}\rangle$ as functions of Ka/π and x/a for $\delta/J = 0.0011$; to obtain the actual interaction strength, $\vec{F}_{K,b}(n_1, n_2)$ needs to be multiplied by $g^2/(N^{1/2}J)$. (a) $\text{Re}[\vec{F}_{K,b}(n_1, n_2)]$ for $U/J = -1$. (b) $\text{Im}[\vec{F}_{K,b}(n_1, n_2)]$ for $U/J = -1$. (c) $\text{Re}[\vec{F}_{K,b}(n_1, n_2)]$ for $U/J = -5/2$. (d) $\text{Im}[\vec{F}_{K,b}(n_1, n_2)]$ for $U/J = -5/2$. The color scheme for each of the four panels is different.

two cases [$K^{(0)}a/\pi = 0.0152$ for Figs. 3(a) and 3(b) and $K^{(0)}a/\pi = 0.0162$ for Figs. 3(c) and 3(d)]. Second, the real part of the effective interactions displays a larger K dependence for $x/a = 0$ than for $x/a > 0$. Third, for fixed Ka/π , the real part of the effective interactions is characterized by an overall falloff that sits on top of small amplitude oscillations. Fourth, the magnitude of the imaginary part of the effective interactions is very small for $Ka/\pi \approx 0$. The separation and wave-vector dependencies of $\vec{F}_{K,b}(n_1, n_2)$ have, as shown in the later sections, a strong impact on the system dynamics.

Section IV shows that the effective interactions $\underline{G}_{K,K'}(n_1, n_2)$ play a non-negligible role for scenarios B and C, corresponding to the horizontal solid and dotted lines in Fig. 2(b). The effective interactions $\underline{G}_{K,K'}(n_1, n_2)$ between two two-photon bound states, one with K and the other with K' , depend—for fixed U/J and δ/J —on Ka , $K'a$, and x/a . Figure 4 shows the real part of $\underline{G}_{K,K'}(n_1, n_2)$ for $\delta/J = 0.0011$ for two different separations, namely, $x = 0$ (top row) and $x/a = 10$ (bottom row). The left and right columns are for $U/J = -1$ and $-5/2$, respectively. The key characteristics are as follows.

(i) The oscillatory structure of the real part of $\underline{G}_{K,K'}(n_1, n_2)$ increases with increasing separation.

(ii) For the on-site interaction and detuning considered, the real part of $\underline{G}_{K,K'}(n_1, n_2)$ is negative; the most negative values are found for $K = K' = 0$ for $x/a = 0$ and 10.

We note that the imaginary part of $\underline{G}_{K,K'}(n_1, n_2)$ (not shown) is zero for $K = K'$.

Since \hat{H}^{adia} is Hermitian [this can be seen readily by inspecting $\underline{G}_{K,K'}(n_1, n_2)$], the population is normalized at all times, i.e., $|c_{ee}(t)|^2 + \sum_K |c_{K,b}(t)|^2 = 1$, and the eigenenergies of \hat{H}^{adia} are real. The validity of the approximations (adiabatic elimination and dropping of scattering states) can thus be assessed in two complementary ways, namely, by comparing the time evolution of, e.g., the initial state $|e, e, \text{vac}\rangle$ under \hat{H} and \hat{H}^{adia} and by comparing the eigen-spectra of \hat{H} and \hat{H}^{adia} . Reference [31] constructed a master

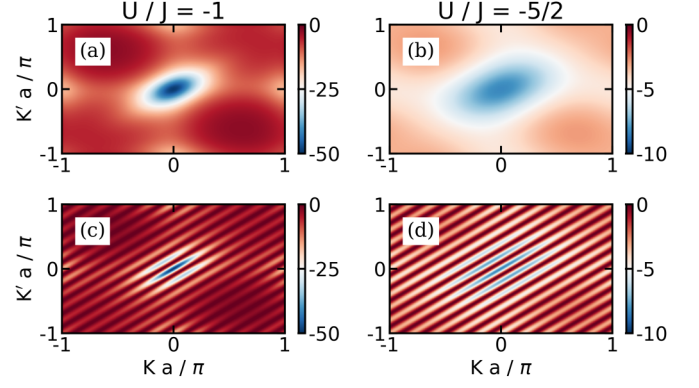


FIG. 4. Contour plots of the real part of the effective dimensionless interactions $\underline{G}_{K,K'}(n_1, n_2)$ between the states $|g, g, K\rangle$ and $|g, g, K'\rangle$ as functions of Ka/π and $K'a/\pi$ for $\delta/J = 0.0011$; to obtain the actual interaction strength, $\underline{G}_{K,K'}(n_1, n_2)$ needs to be multiplied by $g^2/(NJ)$. (a) $\text{Re}[\underline{G}_{K,K'}(n_1, n_2)]$ for $U/J = -1$ and $x/a = 0$. (b) $\text{Re}[\underline{G}_{K,K'}(n_1, n_2)]$ for $U/J = -5/2$ and $x/a = 0$. (c) $\text{Re}[\underline{G}_{K,K'}(n_1, n_2)]$ for $U/J = -1$ and $x/a = 10$. (d) $\text{Re}[\underline{G}_{K,K'}(n_1, n_2)]$ for $U/J = -5/2$ and $x/a = 10$. The color schemes for $U/J = -1$ (a, c) are the same; similarly, the color schemes for $U/J = -5/2$ (b, d) are the same.

equation, using Eq. (28) with $G_{K_i, K_j'}(n_1, n_2) = 0$ as a starting point. We denote \hat{H}^{adia} with $G_{K_i, K_j'}(n_1, n_2) = 0$ and $\neq 0$ by $\hat{H}^{\text{adia},0}$ and $\hat{H}^{\text{adia},1}$, respectively. Section IV shows that $\hat{H}^{\text{adia},1}$ significantly expands the applicability regime of the reduced dimensionality Hamiltonian compared to $\hat{H}^{\text{adia},0}$ in certain parameter regimes.

E. Markov approximation for $\hat{H}^{\text{adia},0}$

For scenario A, the population of the initial state $|e, e, \text{vac}\rangle$ decays approximately exponentially for x/a not too large. As shown in Ref. [31], the decay constant can be determined analytically in this regime using the Markov approximation. Appendix B shows that $\tilde{c}_{ee}(t)$, where $\tilde{c}_{ee}(t)$ denotes the expansion coefficient for the state that rotates with $2\Delta_e$, falls off exponentially according to

$$\tilde{c}_{ee}(t) = \exp(-\Gamma_{\text{bath}}t), \quad (30)$$

where Γ_{bath} is given by

$$\Gamma_{\text{bath}} = \frac{g^4 a}{J^3 \hbar} |F_{K^{(*)}, b}(n_1, n_2)|^2 \rho(K^{(*)}). \quad (31)$$

Here, $K^{(*)}$ is defined through

$$E_{K^{(*)}, b} = 2\hbar\omega_e + 2\Delta_e, \quad (32)$$

with the ‘‘Stark shift’’ $2\Delta_e$ [31],

$$2\Delta_e = -\frac{2}{N} \sum_k \frac{g^2}{\Delta_k}, \quad (33)$$

quantifying the shift of the state $|e, e, \text{vac}\rangle$ due to the ‘‘renormalization’’ by the single-photon states. Correspondingly, the decoupled ($g = 0$) resonance wave number $K^{(0)}$ gets shifted to $K^{(*)}$ for finite g/J ; the use of $K^{(*)}$ in place of $K^{(0)}$, as done in Ref. [31], provides an improved description. The density of

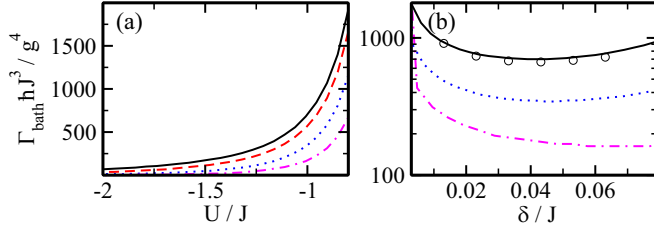


FIG. 5. Lines show the dimensionless decay constant $\Gamma_{\text{bath}} \hbar J^3 / g^4$, obtained within the Markov approximation [Eq. (31)]. (a) The black solid, red dashed, blue dotted, and magenta dash-dotted lines show $\Gamma_{\text{bath}} \hbar J^3 / g^4$ as a function of U/J for $\delta/J = 0.0431$ and $x/a = 0, 2, 4$, and 6 , respectively. (b) The black solid, blue dotted, and magenta dash-dotted lines show $\Gamma_{\text{bath}} \hbar J^3 / g^4$ as a function of δ/J for $U/J = -1$ and $x/a = 0, 4$, and 6 , respectively. For comparison, the open black circles show the decay constant extracted from the dynamics for the full Hamiltonian \hat{H} for $x/a = 0$ and $g/J = 1/50$; the Markov approximation results (solid line) capture the decay constant extracted from the full decay dynamics quite well. Note that the Markov approximation breaks down when δ/J approaches zero (left portion of the panel) and when δ/J approaches the two-photon scattering continuum (right portion of the panel).

states $\rho(K^{(*)})$ at the resonance wave vector can be written as

$$\rho(K^{(*)}) = J(\hbar v_{K^{(*)},b})^{-1}. \quad (34)$$

When $|g/J|$ is not much smaller than 1, the adiabatic elimination and, correspondingly, the concept of a resonant wave number lose their meaning. The importance of the Stark shift $2\Delta_e$ increases as $K^{(0)}a$ and, correspondingly, the detuning δ/J approach zero.

Figures 5(a) and 5(b) show the decay constant $\Gamma_{\text{bath}} \hbar J^3 / g^4$ as a function of the on-site interaction U/J and the detuning δ/J , respectively, for various separations ($x/a = 0$ to 6). It can be seen that the radiation dynamics is characterized by a larger dimensionless decay constant (faster decay) for $x/a = 0$ (solid line) than for $x/a = 6$ (dash-dotted line). This makes sense intuitively since a larger separation is associated with a smaller, in magnitude, effective interaction $F_{K^{(*)},b}(n_1, n_2)$. The dependence on U/J [see Fig. 5(a)] can also be understood readily intuitively. As $|U/J|$ increases, the two-photon bound state becomes more localized and the coupling to the state $|e, e, \text{vac}\rangle$ decreases. The Markov approximation results shown in Fig. 5(a) agree quite well with the decay constants extracted from full numerical calculations (not shown).

The dependence of the dimensionless decay constant, calculated within the Markov approximation, on the detuning is nonmonotonic [see Fig. 5(b)]. The increase of $\Gamma_{\text{bath}} \hbar J^3 / g^4$ as the dimensionless detuning δ/J , for fixed x/a , approaches zero [left part of Fig. 5(b)] is unphysical. This increase is due to the breakdown of the Markov approximation in the vicinity of the bottom of the band, where the density of states of two-photon bound states is large and diverges as $\delta/J \rightarrow 0$. The open circles in Fig. 5(b) show the decay constant for $x/a = 0$, extracted from calculations for the full Hamiltonian \hat{H} . While the agreement with the Markov approximation results is quite good, we note that the full dynamics displays nonexponential characteristics for small δ/J that get “averaged” when fitting to an exponential. The Markov approximation also breaks

down when δ/J becomes too large [right part of Fig. 5(b)]. The reason for this breakdown is that the adiabatic elimination is not valid when $2\hbar\omega_e$ is close to the two-photon scattering continuum.

To recapitulate, we arrived at Eq. (30) by making four distinct approximations: adiabatically eliminating $c_{1k}(t)$ and $c_{2k}(t)$, neglecting the two-photon scattering continuum, neglecting $\underline{G}_{K,K'}(n_1, n_2)$, and making the Markov approximation. It is useful to compare the results obtained for the two-emitter case with nonlinear bath to those for a single emitter [\hat{H} in Eq. (2) with $N_e = 1$ and $U = 0$ with initial state $|e, \text{vac}\rangle$]. Appendix A shows that the decay constant Γ_{single} for the single-emitter system evaluates within the Markov approximation to

$$\Gamma_{\text{single}} = \frac{g^2 a}{\hbar J} \rho_{\text{single}}(k^{(0)}), \quad (35)$$

where

$$\rho_{\text{single}}(k^{(0)}) = J(\hbar v_{k^{(0)}})^{-1}, \quad (36)$$

with $k^{(0)}$ denoting the single-photon resonance wave vector.

Comparison of Eqs. (31) and (35) indicates that the two-emitter dynamics, in the regime where $|c_{ee}(t)|^2$ —starting in the state $|e, e, \text{vac}\rangle$ —falls off exponentially, is the same as that for the single emitter system, provided (i) the dimensionless densities of states $a\rho(K^{(*)})$ and $a\rho_{\text{single}}(k^{(0)})$ take the same value and (ii) the coupling constant g_{single} of the single emitter system is set to

$$g_{\text{single}} = \frac{g^2}{J} |F_{K^{(*)},b}(n_1, n_2)|; \quad (37)$$

the quantities on the right-hand side are understood to be those characterizing the two-emitter system. To match the densities of states, we consider $K^{(*)}a$ and $k^{(0)}a$ values that are sufficiently large for the Markov approximation to hold but sufficiently small for $\Delta_{K,b}$ and E_k to be well approximated by their Taylor-expanded expressions up to order $(Ka)^2$ and $(ka)^2$, respectively. Comparing the slopes of the quadratic terms, we find that the dimensionless densities of states match if the tunneling coupling strength J_{single} of the single emitter system is set to

$$J_{\text{single}} = 2J \left[\left(\frac{U}{J} \right)^2 + 16 \cos^2 \left(\frac{K^{(*)}a}{2} \right) \right]^{-1/2}; \quad (38)$$

the quantities on the right-hand side are, again, understood to be those characterizing the two-emitter system.

The meaning of Eqs. (37) and (38) is as follows. Say we have a coupled two-emitter–cavity system in the Markovian regime. For a given U/J , g/J , δ/J , and x/a , this implies that the exponential decay of the population is characterized by Γ_{bath} . Imagine now that we want to design a coupled single-emitter–cavity system such that the exponential decay of $|d_e(t)|^2$, see Eq. (B1), is characterized by $\Gamma_{\text{single}} = \Gamma_{\text{bath}}$. This goal is accomplished if the tunneling coupling strength J_{single} and coupling strength g_{single} of the single-emitter–cavity system are chosen according to Eqs. (37) and (38).

Using that $|F_{K^{(*)},b}(n_1, n_2)|$ is—for the parameters considered in this paper (see Fig. 3 for two examples)—of the order of 1 to 10, Eq. (37) shows that the two-emitter dynamics considered is slower than the single-emitter dynamics would be

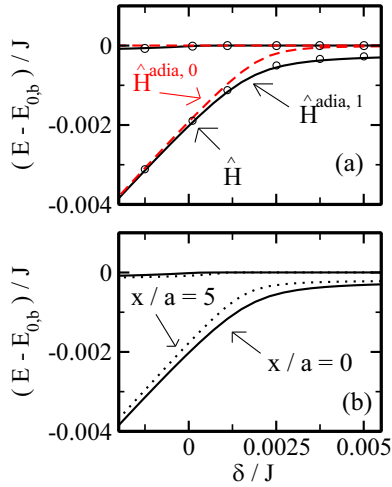


FIG. 6. Energy of the two lowest eigenstates as a function of δ/J for $U/J = -1$ and $g/J = 1/50$. (a) The black solid and red dashed lines show the energy for $\hat{H}^{\text{adia},1}$ and $\hat{H}^{\text{adia},0}$, respectively, for $x/a = 0$. For comparison, the open circles show the eigenenergies for \hat{H} (using a basis that excludes the two-photon scattering states). The energies for \hat{H} and $\hat{H}^{\text{adia},1}$ agree very well. (b) The black solid and black dotted lines show the energies of $\hat{H}^{\text{adia},1}$ for $x/a = 0$ and 5, respectively. A clear separation dependence can be seen. In both panels, the lower state corresponds to a hybridized bound state with appreciable $|e, e, \text{vac}\rangle$ and $|g, g, \text{pol}\rangle$ contributions (see Sec. III B for details).

if the single emitter was in resonance with the single-photon band. Importantly, if the two-emitter energy is in resonance with the two-photon bound-state band, then the single-emitter energy is not in resonance with the single-photon band (at least not for the parameters considered in this paper). We note that appreciable single-emitter dynamics is observed for large x/a for certain parameter combinations (see Sec. IV for details).

III. STATIONARY SOLUTION

This section discusses the stationary solutions of the coupled emitter-cavity system under study. Section III A provides an overview for different detunings while Sec. III B focuses on the physics near the bottom of the band.

A. Overview

To assess the reliability of the different approximations, we compare the energy spectrum obtained by diagonalizing $\hat{H}^{\text{adia},0}$, $\hat{H}^{\text{adia},1}$, and \hat{H} (using a basis that excludes the two-photon scattering states) for $U/J = -1$ for various δ/J . Figure 6(a) shows the lowest two eigenenergies for $x/a = 0$. The zero of the energy axis corresponds to the bottom of the $g = 0$ two-photon energy band. The eigenenergies of the full Hamiltonian (open circles) are reproduced much better by $\hat{H}^{\text{adia},1}$ (black solid lines) than by $\hat{H}^{\text{adia},0}$ (red dashed lines). Specifically, neglecting the effective interactions $\underline{G}_{K,K'}(n_1, n_2)$ leads to a weakening of the binding of the lowest-energy state, especially for positive δ/J . The lowest-energy state is a hybridized bound state that contains contributions from the

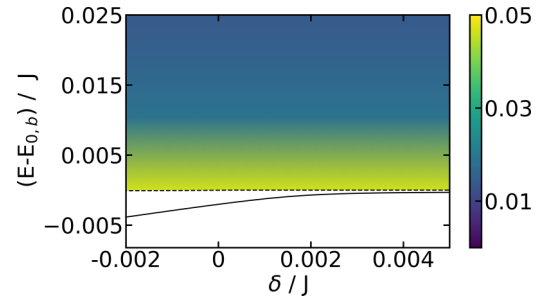


FIG. 7. Visualization of the eigenspectrum of $\hat{H}^{\text{adia},1}$ as a function of the detuning δ/J for $U/J = -1$, $g/J = 1/50$, and $x = 0$. The density of states $\rho_E(E)$ of the continuum portion of the energy spectrum, which is dominated by states that have no or extremely small emitter admixtures, is shown in color (the legend is shown on the right; arbitrary units are used). The lowest hybridized bound state (black solid line) is well separated from the energy continuum. The second lowest state (black dashed line) is separated by a small gap from the continuum for negative δ/J and part of the continuum for positive δ/J .

state $|e, e, \text{vac}\rangle$ and two-photon bound states. The hybridized state is clearly separated from the energy continuum. The character of the lowest-energy eigenstate is elucidated in the next section.

The density of states $\rho_E(E)$ (number of states per unit energy interval) of the energy continuum, which reduces to the two-photon bound-state band for $g = 0$, is shown by the color map in Fig. 7 for the same parameters as those used in Fig. 6(a). The density of states is large near the bottom of the energy band and decreases as one moves away from the bottom of the band. While the coupling constant g has a profound effect on the two lowest eigenstates (black solid and dashed lines in Fig. 7), the density of states depends comparatively weakly on g .

To elucidate the dependence on the separation for $U/J = -1$, we work with $\hat{H}^{\text{adia},1}$. Figure 6(b) shows the two lowest eigenenergies as a function of δ/J for $x/a = 0$ (solid line) and $x/a = 5$ (dotted line). The binding energy of the lowest hybridized bound state decreases with increasing x/a . This might be expected naively since a larger emitter separation is associated with reduced interactions. Interestingly, the second-lowest-energy state has a somewhat lower energy for $x/a = 5$ than for $x/a = 0$; this can be seen most clearly in Fig. 6(b) for negative detuning but also holds true for positive δ/J . An analysis of the corresponding eigenstate reveals that the second lowest state for $x/a = 5$ has bound-state character not only for negative but also for positive detuning. For $x/a = 0$, in contrast, the second lowest state merges into the continuum when the detuning is positive. The emergence of a second bound state with increasing separation is somewhat counterintuitive. We checked that the full Hamiltonian \hat{H} also supports a second bound state, i.e., we checked that its appearance is not an artifact of the adiabatic approximation. To gain additional insights, the next section discusses a two-state model that captures key aspects of the two hybridized bound states that exist for $U/J = -1$, small detuning, and sufficiently large x/a .

B. Near the bottom of the band: Two-state model

An important conclusion of the previous section is that the adiabatic Hamiltonian $\hat{H}_b^{\text{adia},1}$ captures the key features of the bound states supported by the full Hamiltonian \hat{H} . Using $\hat{H}_b^{\text{adia},1}$, we now review the physical picture that was introduced in Ref. [32]. Since the effective interactions $\underline{G}_{K,K'}(n_1, n_2)$ cannot be neglected near the bottom of the band (see the previous section), the bath Hamiltonian contains off diagonals in the $\{|g, g, K\rangle, |e, e, \text{vac}\rangle\}$ basis. To proceed, we change the basis. We continue to use $|g, g\rangle$ and $|e, e\rangle$ with energy 0 and $2\Delta_e$, respectively, for the two emitters. For the two-photon bath Hamiltonian, in contrast, we change from the basis states $|K\rangle$, in which the bath is characterized by effective interactions between two-photon bound states with center-of-mass wave numbers K and K' ,

$$\underline{H}_b^{\text{adia},1} = \underline{\Delta}_{K,b} + \frac{g^2}{JN} \underline{G}_{K,K'}(n_1, n_2), \quad (39)$$

to a basis in which the bath Hamiltonian $\hat{H}_b^{\text{adia},1}$ is diagonal. Performing the diagonalization, we find that the energy spectrum of the adiabatic bath Hamiltonian $\hat{H}_b^{\text{adia},1}$ consists of a continuum, similar to the two-photon bound-state band, and an ‘‘isolated state’’ the energy of which is energetically separated from the bottom of the two-excitation continuum; this state lives in the band gap and corresponds to a bound state.

The isolated state $|\text{pol}\rangle$ is well reproduced by an ansatz with Lorentzian distributed expansion coefficients d_K [32]:

$$|\text{pol}\rangle = \sum_K d_K |K\rangle \quad (40)$$

and

$$d_K = \frac{(2L_{\text{eff}}^{-1}a)^{3/2}}{\sqrt{N}} \frac{1}{(2Ka)^2 + (L_{\text{eff}}^{-1}a)^2}, \quad (41)$$

where the normalization is chosen such that

$$a \int_{-\infty}^{\infty} |d_K|^2 dK = 1. \quad (42)$$

In writing this ansatz, it is assumed that $L_{\text{eff}}^{-1}a$ is much smaller than π so that the integration limits can be safely extended from $\pm\pi$ to $\pm\infty$. We refer to the isolated state as a polaronlike state as it represents a quasiparticle that is a superposition of states with different center-of-mass momenta. The wave-number width of the expansion coefficients d_K is given by $(L_{\text{eff}})^{-1}$. We determine L_{eff} by minimizing the ground-state energy of $\hat{H}_b^{\text{adia},1}$. To make the calculations tractable analytically, we approximate the effective interactions $\underline{G}_{K,K'}(n_1, n_2)$ by a constant, namely, their value at $K = K' = K^{(0)}$. We find

$$\frac{L_{\text{eff}}}{a} = \frac{2J^3}{g^2 |G_{K^{(0)},K^{(0)}}(n_1, n_2)| \sqrt{U^2 + 16J^2}} \quad (43)$$

and

$$E_{\text{pol}} = -\delta - \frac{g^4}{8J^4} |G_{K^{(0)},K^{(0)}}(n_1, n_2)|^2 \sqrt{U^2 + 16J^2}. \quad (44)$$

This variational result reproduces the numerically determined ground-state energy of $\hat{H}_b^{\text{adia},1}$ very well. In the condensed-matter context, the Hamiltonian that supports the polaronlike

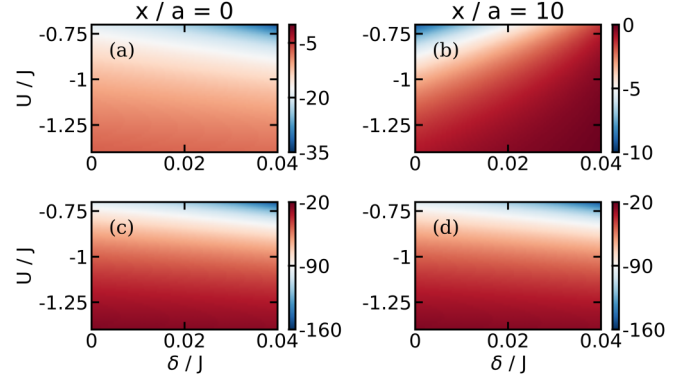


FIG. 8. Contour plots of the effective dimensionless interaction $F_{K^{(0)},b}(n_1, n_2)$ between the states $|e, e, \text{vac}\rangle$ and $\hat{P}_{K^{(0)},b}^\dagger |g, g, \text{vac}\rangle$ and the effective dimensionless interaction $G_{K^{(0)},K^{(0)}}(n_1, n_2)$ between the states $|g, g, K^{(0)}\rangle$ and $|g, g, K^{(0)}\rangle$ as functions of δ/J and U/J ; to obtain the actual interaction strengths, $F_{K^{(0)},b}(n_1, n_2)$ and $G_{K^{(0)},K^{(0)}}(n_1, n_2)$ need to be multiplied by $g^2/(N^{1/2}J)$ and $g^2/(NJ)$, respectively. (a) $\text{Re}[F_{K^{(0)},b}(n_1, n_2)]$ for $x/a = 0$. (b) $\text{Re}[F_{K^{(0)},b}(n_1, n_2)]$ for $x/a = 10$. (c) $\text{Re}[G_{K^{(0)},K^{(0)}}(n_1, n_2)]$ for $x/a = 0$. (d) $\text{Re}[G_{K^{(0)},K^{(0)}}(n_1, n_2)]$ for $x/a = 10$. The color schemes for $\text{Re}[F_{K^{(0)},b}(n_1, n_2)]$ are different for the two separations. The color schemes for $\text{Re}[G_{K^{(0)},K^{(0)}}(n_1, n_2)]$, in contrast, are the same for the two separations.

state shows up when an impurity or defect in a one-dimensional lattice is associated with attractive all-to-all momentum space interactions. All-to-all interactions are currently being investigated by a number of groups due to their relevance in quantum gravity and spin-glass physics [49–51].

As already alluded to in Sec. IID, the effective interactions $\underline{G}_{K,K'}(n_1, n_2)$ are purely real for $K = K'$. Figures 8(c) and 8(d) show $\text{Re}[G_{K^{(0)},K^{(0)}}(n_1, n_2)]$ as functions of δ/J and U/J for $x/a = 0$ and 10, respectively. It can be seen that $G_{K^{(0)},K^{(0)}}(n_1, n_2)$ depends extremely weakly on the separation x/a . Consequently, the energy E_{pol} of the photonic polaron is to a very good approximation independent of the emitter separation x/a .

Next, we rewrite $\hat{H}_b^{\text{adia},1}$ in the product basis in which the emitter and bath Hamiltonians are diagonal. Transforming the system-bath coupling $g^2 N^{-1/2} \hat{F}_{K,b}(n_1, n_2)/J$ to the new basis and restricting the Hilbert space to the states $|e, e, \text{vac}\rangle$ and $|g, g, \text{pol}\rangle$, we arrive at the following matrix representation of the two-state Hamiltonian $\hat{H}^{2\text{-st}}$:

$$\underline{H}^{2\text{-st}} = \begin{pmatrix} 2\Delta_e & G_{\text{eff}}(n_1, n_2) \\ [G_{\text{eff}}(n_1, n_2)]^* & E_{\text{pol}} \end{pmatrix}. \quad (45)$$

Using our variational expression for $|g, g, \text{pol}\rangle$, the effective coupling $G_{\text{eff}}(n_1, n_2)$ between states $|e, e, \text{vac}\rangle$ and $|g, g, \text{pol}\rangle$ can be written as

$$G_{\text{eff}}(n_1, n_2) = \frac{g^3 (U^2 + 16J^2)^{1/4}}{2J^{5/2}} \times F_{K^{(0)},b}(n_1, n_2) |G_{K^{(0)},K^{(0)}}(n_1, n_2)|^{1/2}. \quad (46)$$

Figures 8(a) and 8(b) show $\text{Re}[F_{K^{(0)},b}(n_1, n_2)]$ as functions of δ/J and U/J for $x/a = 0$ and 10, respectively. It can be seen that $\text{Re}[F_{K^{(0)},b}(n_1, n_2)]$ [Figs. 8(a) and 8(b)] varies much more

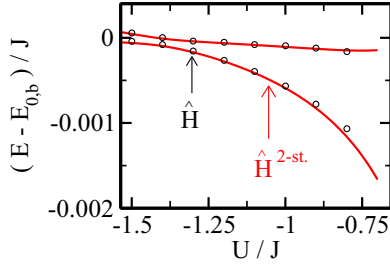


FIG. 9. Energy of the hybridized states as a function of U/J for $g/J = 1/50$, $\delta/J = 0.0011$, and $x/a = 10$. The black circles and red lines are obtained using the full Hamiltonian \hat{H} and the two-state Hamiltonian $\hat{H}^{2\text{-st}}$, respectively. The agreement is very good for the parameter regime considered.

strongly with x/a than $\text{Re}[G_{K^{(0)}, K^{(0)}}(n_1, n_2)]$ [Figs. 8(c) and 8(d)]. We conclude that, in the regime where the two-state model $\hat{H}^{2\text{-st}}$ provides a faithful description, the separation dependence of the hybridized energy eigenstates of \hat{H} (see the discussion surrounding Figs. 6 and 7) is due to the dependence of $G_{\text{eff}}(n_1, n_2)$ on $F_{K^{(0)}, b}(n_1, n_2)$.

The eigenstates Ψ_{\pm} and eigenenergies E_{\pm} of $\hat{H}^{2\text{-st}}$ read

$$\Psi_{\pm} = d_{\text{vac}}^{(\pm)} |e, e, \text{vac}\rangle + d_{\text{pol}}^{(\pm)} |g, g, \text{pol}\rangle \quad (47)$$

and

$$E_{\pm} = \left(\Delta_e + \frac{E_{\text{pol}}}{2} \right) \pm \sqrt{\left(\Delta_e - \frac{E_{\text{pol}}}{2} \right)^2 + |G_{\text{eff}}|^2}, \quad (48)$$

where the expansion coefficients $d_{\text{vac}}^{(\pm)}$ and $d_{\text{pol}}^{(\pm)}$ are given by

$$d_{\text{vac}}^{(\pm)} = N_{\pm} G_{\text{eff}} \quad (49)$$

and

$$d_{\text{pol}}^{(\pm)} = N_{\pm} \left(-\Delta_e + \frac{E_{\text{pol}}}{2} \pm \sqrt{\left(\Delta_e - \frac{E_{\text{pol}}}{2} \right)^2 + |G_{\text{eff}}|^2} \right), \quad (50)$$

respectively; in Eqs. (49) and (50), N_+ and N_- denote normalization constants. We refer to Ψ_+ and Ψ_- as the symmetric hybridized state and antisymmetric hybridized state, respectively.

Figure 9 compares the two eigenenergies supported by $\hat{H}^{2\text{-st}}$ (red solid lines) for $\delta/J = 0.0011$ and $x/a = 10$ with the two eigenenergies of \hat{H} , the eigenstates of which have the largest overlap with the initial state $|e, e, \text{vac}\rangle$ (black circles), as a function of U/J . The two-state model reproduces the energy of the hybridized energy eigenstates of the full Hamiltonian well. The state Ψ_- is bound for $|U/J|$ values smaller than 1.4 and unbound for $|U/J|$ values larger than 1.4. Since a strong on-site interaction (large $|U/J|$) corresponds to more localized two-photon bound states (in real space), the “reach” of the two-photon bound state for large $|U/J|$ is too small to induce a new bound state. As discussed in the next section, the two-state Hamiltonian $\hat{H}^{2\text{-st}}$ describes several key characteristics of the dynamics predicted by the full Hamiltonian in the $|\delta/J| \rightarrow 0$ limit.

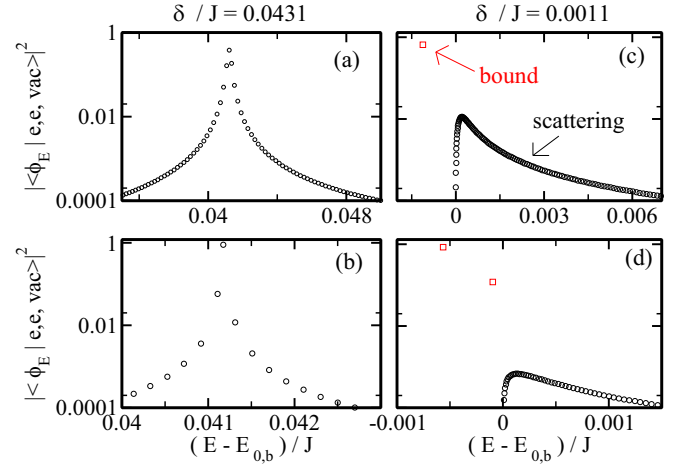


FIG. 10. Projection of the initial state $|e, e, \text{vac}\rangle$ onto the energy eigenstates ϕ_E of \hat{H} for $U/J = -1$ and $g/J = 1/50$. The square of the absolute value of the overlap onto scattering states and bound states is shown by black circles and red squares, respectively, for (a) $\delta/J = 0.0431$ and $x/a = 0$, (b) $\delta/J = 0.0431$ and $x/a = 10$, (c) $\delta/J = 0.0011$ and $x/a = 0$, and (d) $\delta/J = 0.0011$ and $x/a = 10$.

IV. DYNAMICS

This section discusses the radiation dynamics for $U/J = -1$ for various detunings δ/J and separations x/a . Throughout, the initial state is taken to be the excited emitter state $|e, e, \text{vac}\rangle$. Figure 10 shows the decomposition of the state $|e, e, \text{vac}\rangle$ into the energy eigenstates ϕ_E of \hat{H} for $U/J = -1$ and two different separations, namely, $x/a = 0$ (top row) and $x/a = 10$ (bottom row). Two different detunings are considered: $\delta/J = 0.0431$ (left column) and $\delta/J = 0.0011$ (right column). As discussed in Sec. II E, the Markov approximation provides a good description of the radiation dynamics for $\delta/J = 0.0431$ but breaks down for $\delta/J = 0.0011$. For the larger detuning, the initial state is dominated by a few eigenstates the energy of which is close to those corresponding to $K^{(*)}$. The applicability of the Markov approximation relies on the fact that the overlap coefficients peak around one energy value and fall off quickly away from this energy. We emphasize that the overall behavior of the overlap coefficients for $x/a = 0$ [Fig. 10(a)] and $x/a = 10$ [Fig. 10(b)] is similar. Note, however, that the scale of the energy axis and the number of eigenstates that contribute are significantly smaller for $x/a = 10$ than for $x/a = 0$.

As the detuning decreases to small positive values, where the two-emitter energy is very close to the bottom of the energy band, the decomposition of the initial state into the energy eigenstates changes significantly. For $x/a = 0$, the initial state is dominated by a single state [red square in Fig. 10(c)] the energy of which is separated from the energy continuum (round circles). Altogether, the states corresponding to the energy continuum contribute 34.5%. For $x/a = 10$, in contrast, there are two energy eigenstates that contribute appreciably [84.6 and 12.0%; see red squares in Fig. 10(d)]. The eigenstates corresponding to the red squares in Figs. 10(c) and 10(d) are quite well described by the two-state model Hamiltonian $\hat{H}^{2\text{-st}}$, Eq. (45).

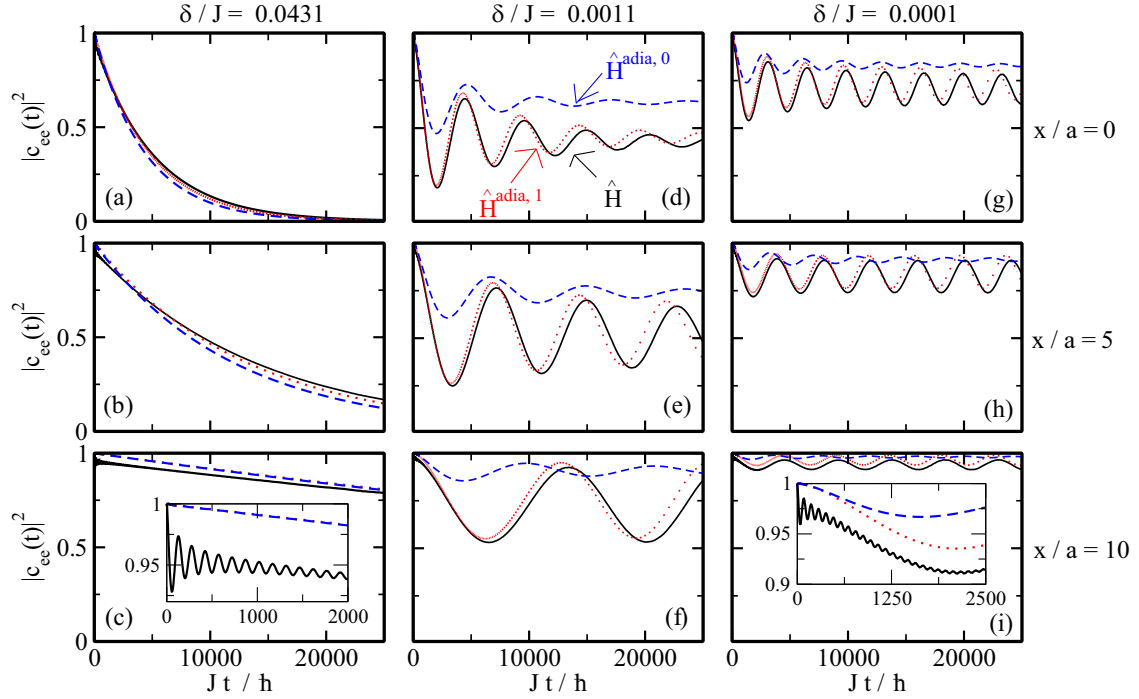


FIG. 11. Radiation dynamics for the initial state $|e, e, \text{vac}\rangle$, $U/J = -1$, and $g/J = 1/50$. The lines show the population $P_{ee}(t)$ for various x/a and δ/J . The value of x/a increases from the top row to the bottom row ($x/a = 0, 5$, and 10 for the first, second, and third row, respectively). The value of δ/J decreases from the leftmost to the rightmost column ($\delta/J = 0.0431, 0.0011$, and 0.0001 for the first, second, and third column, respectively). In all panels, the solid, dotted, and dashed lines show $P_{ee}(t)$ obtained by propagating the initial state $|e, e, \text{vac}\rangle$ under the Hamiltonian \hat{H} , $\hat{H}^{\text{adia},1}$, and $\hat{H}^{\text{adia},0}$, respectively. The data shown in panels (a)–(f) are also shown in Ref. [32].

Figure 11 shows the time evolution of the population $P_{ee}(t)$ of state $|e, e, \text{vac}\rangle$ for $U/J = -1$. For $\delta/J = 0.0431$ (left column), $P_{ee}(t)$ falls off roughly exponentially. The decay is faster for $x/a = 0$ [Fig. 11(a)] than for $x/a = 5$ and 10 [Figs. 11(b) and 11(c)]. For this large δ/J , the Markov approximation works well and the agreement between the results for \hat{H} (solid lines), $\hat{H}^{\text{adia},1}$ (dotted lines), and $\hat{H}^{\text{adia},0}$ (dashed lines) is quite good. For $x/a = 0, 5$, and 10 , the population of the single-photon states (i.e., the sum of $\sum_{j=1,2} \sum_k |c_{jk}|^2$) is approximately equal to $1.8, 2.0$, and 4.0% , respectively. The comparatively large population of the single-photon states for $x/a = 10$ signals that the adiabatic elimination deteriorates for large x/a . The inset of Fig. 11(c) shows that the radiation emitted by the first and second emitters are uncorrelated initially. We find that the oscillations displayed by the black solid line are well reproduced by the single-emitter dynamics, i.e., by treating the two emitters as independent quantities (effectively, this corresponds to setting $U = 0$).

For small δ/J , the dynamics changes significantly. The middle and rightmost columns of Fig. 11 correspond to $\delta/J = 0.0011$ and 0.0001 , respectively. For these two detunings, the population $P_{ee}(t)$ does not change exponentially but instead exhibits damped or essentially undamped oscillatory behaviors for $x/a = 0, 5$, and 10 . For all six parameter combinations [Figs. 11(d)–(i)], the adiabatic elimination Hamiltonian $\hat{H}^{\text{adia},1}$ (red dotted lines), which accounts for the effective interactions $\underline{G}_{K,K'}(n_1, n_2)$, reproduces the key features of the dynamics of the full Hamiltonian \hat{H} (black solid line)—such as the amplitude, frequency, and degree of damping—faithfully. The

adiabatic elimination Hamiltonian $\hat{H}^{\text{adia},0}$ (blue dashed lines), in contrast, provides a comparatively poor description of the oscillatory dynamics [Figs. 11(d)–(i)]. The comparison shows that appearance of essentially undamped oscillations depends critically on the effective interactions $\underline{G}_{K,K'}(n_1, n_2)$; recall, these are not included in $\hat{H}^{\text{adia},0}$. The inset of Fig. 11(i) illustrates, as for the larger detuning, that the elimination of the single-photon states from the Hilbert space does remove fast oscillations and fails to capture the initial decay of $P_{ee}(t)$ that is due to uncorrelated decay of single photons.

Figure 12 shows the populations $|c_{K,b}(t)|^2$ of the two-photon states $|g, g, K\rangle$ as functions of Jt/\hbar and Ka/π for $\delta/J = 0.0431$ (top row) and $\delta/J = 0.0011$ (bottom row). The behavior for large and small detunings is distinct. For $\delta/J = 0.0431$, a few Ka/π values—centered around $K^{(*)}a/\pi$ —get populated as time increases for $x/a = 0$ [Fig. 12(a)] and $x/a = 10$ [Fig. 12(c)]. The excitations, which exist initially in the form of matter, get transferred to the photons. Since the decay involves multiple states, the radiation emitted is incoherent. For $\delta/J = 0.0011$, the populations $|c_{K,b}(t)|^2$ with $K \approx 0$ oscillate in time for $x/a = 0$ [Fig. 12(b)] and $x/a = 10$ [Fig. 12(d)]. As expected, the oscillation frequencies are the same as those displayed in Figs. 11(d) and 11(f).

The undamped Rabi oscillations displayed in Fig. 11 are readily explained by the fact that the Hamiltonian \hat{H} supports two bound states for sufficiently large x/a . The initial state can, to a good approximation be written as a superposition of the symmetric and antisymmetric hybridized energy eigenstates Ψ_+ and Ψ_- . As a function of time, population is

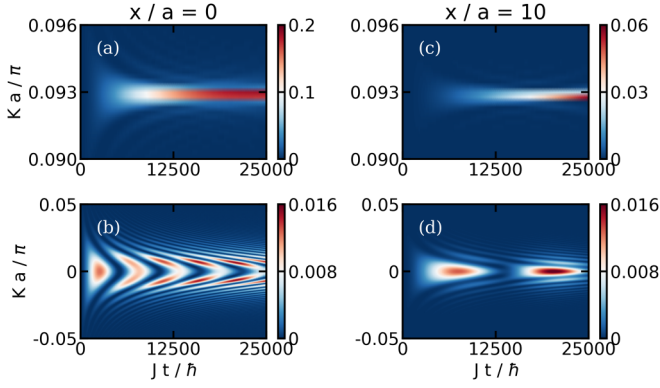


FIG. 12. Contour plot of the populations $|c_{K,b}(t)|^2$ of the two-photon bound states $|g, g, K\rangle$ as functions of the dimensionless center-of-mass wave number Ka/π and the dimensionless time Jt/\hbar for $U/J = -1$ and $g/J = 1/50$. (a) $\delta/J = 0.0431$ and $x/a = 0$. (b) $\delta/J = 0.0011$ and $x/a = 0$. (c) $\delta/J = 0.0431$ and $x/a = 10$. (d) $\delta/J = 0.0011$ and $x/a = 10$. The color scheme and range of the vertical axis are adjusted in each panel for ease of viewing.

transferred between the two bound energy eigenstates, with the angular oscillation frequency being equal to $(E_- - E_+)/\hbar$.

To explain the damping, we decompose the initial state $|e, e, \text{vac}\rangle$ into the energy eigenstates ϕ_E of \hat{H} . For this calculation, we divide the energy eigenstates into two groups: the state ϕ_0 with energy E_0 (lowest-energy eigenstate) and the states $\{\phi_j\}$ with energy E_j ($j = 1, 2, \dots$; all other states). The latter group of states includes the scattering states and the hybridized state Ψ_- , the energy of which is either just below or immersed into the scattering continuum. Using this grouping, we find

$$|c_{ee}(t)|^2 \approx (P_0)^2 + 2P_0 \sum_{j>0} P_j \cos \left[\frac{(E_0 - E_j)t}{\hbar} \right], \quad (51)$$

where the time-independent probabilities P_j are given by

$$P_j = |\langle e, e, \text{vac} | \phi_j \rangle|^2 \quad (52)$$

(the P_j are positive). In writing Eq. (51), we dropped the term $C(t)$,

$$C(t) = \sum_{j>0, j'>0} P_j P_{j'} \cos \left[\frac{(E_j - E_{j'})t}{\hbar} \right], \quad (53)$$

on the right-hand side; we find numerically that the term $C(t)$ contributes negligibly to $|c_{ee}(t)|^2$. The damping of the Rabi oscillations is thus due to the energy spread of the energy states ϕ_j ($j > 0$) with nonvanishing P_j . We refer to this as dephasing.

If we replace the energies E_j with $j > 0$ in Eq. (51) by E_- , we find

$$|c_{ee}(t)|^2 \approx (P_0)^2 + 2P_0(1 - P_0) \cos \left[\frac{(E_0 - E_-)t}{\hbar} \right]. \quad (54)$$

The fractional population [52], i.e., the large t limit of $|c_{ee}(t)|^2$, is to a very good approximation given by $(P_0)^2$. Equation (54) describes undamped Rabi oscillations, which reproduce the short-time amplitude and oscillation frequency very well (see Fig. 13). The damping, which is due—

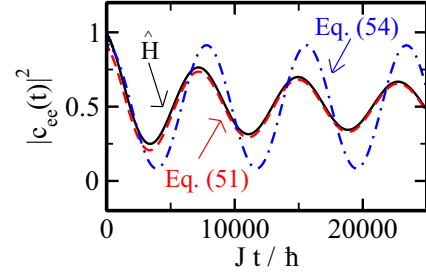


FIG. 13. Population $P_{ee}(t) = |c_{ee}(t)|^2$ as a function of time for $U/J = -1$, $g/J = 1/50$, $\delta/J = 0.0011$, and $x/a = 5$. The black solid line shows $P_{ee}(t)$ obtained by propagating the initial state $|e, e, \text{vac}\rangle$ under the Hamiltonian \hat{H} . The red dashed and blue dash-dotted lines show $P_{ee}(t)$ obtained using Eqs. (51) and (54), respectively.

already pointed out above—to the energy spread of the E_j with $j > 1$, is not captured by Eq. (54). Alternatively, the damping can be explained by using that the hybridized state Ψ_- , supported by \hat{H} and $\hat{H}^{\text{adia},1}$, is for small x/a immersed in the scattering continuum. As such, its energy acquires an imaginary part, which provides a finite lifetime or damping coefficient.

V. CONCLUSION

This paper discussed the dynamics of two emitters coupled to a waveguide with Kerr-like nonlinearity. Our interest was in the regime where the two emitters are in resonance with the two-photon bound state supported by the one-dimensional waveguide. Even though the emitters are not interacting with each other, correlated dynamics is introduced through the coupling of the emitters to the waveguide. The induced correlations occur on length scales that are comparable to the size of the two-photon bound state. Somewhat surprisingly, a regime where the excitations are transferred back and forth between the emitter and photonic degrees of freedom is observed. The essentially undamped Rabi oscillations are due to the emergence of two hybridized bound states the energies of which lie in the band gap. This behavior is unique to the two-emitter system: the single-emitter system does not display an analogous behavior.

Throughout, we worked in the weak-coupling regime; specifically, the figures all use a coupling strength of $g/J = 1/50$. In the Markovian regime [scenario A; see Fig. 2(b)], the coupling constant enters as a multiplicative factor, i.e., the decay constant Γ_{bath} is directly proportional to $(g/J)^4$ [see Eq. (31)]. This regime had previously been investigated in Ref. [31]. For resonance wave vectors $K^{(*)}$ near the bottom of the band [scenarios B and C; see Fig. 2(b)], the g dependence is more intricate. Within the two-state Hamiltonian $\hat{H}^{2\text{-st}}$, the coupling constant enters through Δ_e , E_{pol} , and $G_{\text{eff}}(n_1, n_2)$: Δ_e is directly proportional to $-(g/J)^2$, E_{pol} contains a term that is proportional to $-(g/J)^4$, and $G_{\text{eff}}(n_1, n_2)$ is directly proportional to $(g/J)^3$. Because of this nontrivial g dependence, the energies of the hybridized eigenstates and, correspondingly, the Rabi oscillation frequency vary notably with g/J . In addition, the regime where the two-state Hamiltonian $\hat{H}^{2\text{-st}}$ provides a reliable description depends on g/J . For g/J

values that are smaller than the value considered in this paper, the observation of Rabi oscillations requires smaller detuning δ/J . Conversely, a larger g/J allows for the observation of Rabi oscillations for larger δ/J . It is an open question how large g/J can be before counter-rotating terms, which are not included in \hat{H} , play a non-negligible role. We are not aware of any previous work on cavity arrays with Kerr-like nonlinearity coupled to two-level emitters that looked at parameter combinations corresponding to scenarios B and C. As shown in this paper, these scenarios give rise to qualitatively new behaviors that are inaccessible in the absence of the nonlinearity and in cavity array–single-emitter systems.

Our treatment neglects, as already pointed out in the last paragraph of Sec. II A, single-photon losses. If the single-photon loss rate is denoted by κ , the exponential decay for the initial state $|e, \text{vac}\rangle$ is characterized by Γ_1 , where $\Gamma_1 = \kappa g^2/[4J^{1/2}(\hbar\omega_c - 2J - \hbar\omega_e)^{3/2}]$ [16]. For the dynamics to be dominated by correlated two-photon processes, we must thus require $\Gamma_1 \ll \Gamma_{\text{bath}}$ or, dropping all factors that are (roughly) of order 1, $\hbar\kappa/J \ll (g/J)^2$. Reference [31] argues that this regime can be reached with nonlinear photonic lattices or superconducting qubits coupled to an array of microwave resonators. Recent experimental work on two transmon qubits coupled to a superconducting microwave photonic crystal, e.g., demonstrated tunable on-site and interbound-state interactions [53].

The results presented open the door for several follow-up investigations. Continuing to work in the two-excitation subspace, it would be interesting to consider an emitter array coupled to the nonlinear waveguide. Intriguing hopping dynamics of the radiation might be observed when the radiation is initially localized in two of the emitters. In addition, it might be interesting to investigate the dependence of the dynamics on the initial state. For example, it might be interesting to compare the dynamics for initial states that can be written as product states to that for entangled superposition states.

ACKNOWLEDGMENTS

Support by the National Science Foundation through Grant No. PHY-1806259 is gratefully acknowledged. This work used the Supercomputing Center for Education and Research at the University of Oklahoma.

APPENDIX A: SINGLE-EMITTER DYNAMICS

Section IV uses the dynamics of a single emitter coupled to cavity n as a reference. This Appendix summarizes the single-emitter results. Note that the results are independent of n since the emitter position does not matter.

We expand the time-dependent wave packet as [52,54]

$$|\psi(t)\rangle = \exp(-i\omega_e t) \left[d_e(t)|e, \text{vac}\rangle + \sum_k d_k(t)\hat{a}_k^\dagger|g, \text{vac}\rangle \right], \quad (\text{A1})$$

where $d_e(t)$ and $d_k(t)$ are expansion coefficients. Starting at time $t = 0$ in the state $|e, \text{vac}\rangle$ [i.e., setting $d_e(0) = 1$ and

$d_k(0) = 0$] and following the steps of Ref. [52], one finds

$$\dot{d}_e(t) = - \int_0^t d_e(t-t')\mathcal{M}(t')dt', \quad (\text{A2})$$

where

$$\mathcal{M}(t') = \frac{g^2}{\hbar^2 N} \sum_k \exp\left(-\frac{i\Delta_k t'}{\hbar}\right). \quad (\text{A3})$$

The integral in Eq. (A2) can be evaluated analytically [54].

In what follows, we review results obtained within the Markov approximation [52,54]. The presence of the bath memory function $\mathcal{M}(t')$ in Eq. (A2) indicates that the dynamics is, in general, non-Markovian: the evolution of the coefficient $d_e(t)$ depends on the past, i.e., the system's state at earlier times. If the bath memory time τ_{bath} is short, i.e., if

$$\left| \frac{\dot{d}_e(t)}{d_e(t)} \tau_{\text{bath}} \right| \ll 1, \quad (\text{A4})$$

the Markov approximation

$$\int_0^t \mathcal{M}(t')d_e(t-t')dt' \approx d_e(t) \int_0^t \mathcal{M}(t')dt' \quad (\text{A5})$$

should be reliable. Using

$$\text{Re} \left[\lim_{t \rightarrow \infty} \int_0^t \exp\left(-\frac{i\Delta_k t'}{\hbar}\right) dt' \right] = \pi \hbar \delta(\Delta_k) \quad (\text{A6})$$

and dropping the imaginary part, which introduces a negligible energy shift Δ_{single} , Eq. (A2) can be rewritten as

$$\dot{d}_e(t) = -\Gamma_{\text{single}} d_e(t) \quad (\text{A7})$$

or

$$d_e(t) = \exp(-\Gamma_{\text{single}} t), \quad (\text{A8})$$

where

$$\Gamma_{\text{single}} = \frac{\pi g^2}{\hbar N} \sum_k \delta(\Delta_k). \quad (\text{A9})$$

Equation (A7) describes the effect of the bath on the expansion coefficient of the state $|e, \text{vac}\rangle$. The emitter-bath coupling induces an exponential decay of the population, with a decay rate $2\Gamma_{\text{single}}$, and an energy shift Δ_{single} in the energy of the state $|e, \text{vac}\rangle$.

To find an explicit expression for Γ_{single} , we replace the sum over k by an integral,

$$\sum_k (\dots) = \frac{Na}{2\pi} \int_{-\pi/a}^{\pi/a} (\dots) dk, \quad (\text{A10})$$

and perform a change of variable:

$$dk = \frac{\partial k}{\partial E_k} dE_k = \left(\frac{\partial E_k}{\partial k} \right)^{-1} dE_k. \quad (\text{A11})$$

Defining the density of states $\rho_{\text{single}}(k)$ through

$$\rho_{\text{single}}(k) = J \left(\frac{\partial E_k}{\partial k} \right)^{-1} \quad (\text{A12})$$

and using Eqs. (A10)–(A12) in Eq. (A9), we find

$$\Gamma_{\text{single}} = \frac{g^2 a}{\hbar J} \int_{\hbar\omega_c - 2J}^{\hbar\omega_c + 2J} \delta(E_k - \hbar\omega_e) \rho_{\text{single}}(k) dE_k. \quad (\text{A13})$$

Evaluating the integral yields Eq. (35) from the main text.

APPENDIX B: DETAILS ON ADIABATIC ELIMINATION

Equations (16)–(19) of the main text are equivalent to the time-dependent Schrödinger equation within the two-excitation subspace. After adiabatic elimination, the equations reduce to

$$i\hbar\dot{c}_{ee}(t) = 2\Delta_e c_{ee}(t) + \frac{g^2}{J\sqrt{N}} \sum_K F_{K,b}(n_1, n_2) c_{K,b}(t) + \frac{g^2}{J\sqrt{N}} \sum_K \sum_q F_{K,q}(n_1, n_2) c_{K,q}(t), \quad (\text{B1})$$

$$i\hbar\dot{c}_{K,b}(t) = \Delta_{K,b} c_{K,b}(t) + \frac{g^2}{J\sqrt{N}} F_{K,b}^*(n_1, n_2) c_{ee}(t) + \frac{g^2}{JN} \sum_{K',K} G_{K,K'}(n_1, n_2) c_{K',b}(t) + \frac{g^2}{JN} \sum_{K'} \sum_q H_{K,K',q}(n_1, n_2) c_{K',q}(t), \quad (\text{B2})$$

and

$$i\hbar\dot{c}_{K,q}(t) = \Delta_{K,q} c_{K,q}(t) + \frac{g^2}{J\sqrt{N}} F_{K,q}^*(n_1, n_2) c_{ee}(t) + \frac{g^2}{JN} \sum_{K',K} \sum_{q',q} [H_{K',K,q'}(n_1, n_2)]^* c_{K',b}(t) + \frac{g^2}{JN} \sum_{K',K} \sum_{q',q} J_{K,K',q,q'}(n_1, n_2) c_{K',q'}(t), \quad (\text{B3})$$

where

$$F_{K,b}(n_1, n_2) = - \sum_k \sum_{\alpha=1,2} \frac{J}{N\Delta_k} \exp(-ikan_{\beta(\alpha)}) [M_b(k, n_{\alpha}, K)]^*, \quad (\text{B4})$$

$$F_{K,q}(n_1, n_2) = - \sum_k \sum_{\alpha=1,2} \frac{J}{N\Delta_k} \exp(-ikan_{\beta(\alpha)}) [M_q(k, n_{\alpha}, K)]^*, \quad (\text{B5})$$

$$G_{K,K'}(n_1, n_2) = - \sum_k \sum_{\alpha=1,2} \frac{J}{N\Delta_k} [M_b(k, n_{\alpha}, K)]^* M_b(k, n_{\alpha}, K'), \quad (\text{B6})$$

$$H_{K,K',q}(n_1, n_2) = - \sum_k \sum_{\alpha=1,2} \frac{J}{N\Delta_k} [M_b(k, n_{\alpha}, K)]^* M_q(k, n_{\alpha}, K'), \quad (\text{B7})$$

$$J_{K,K',q,q'}(n_1, n_2) = - \sum_k \sum_{\alpha=1,2} \frac{J}{N\Delta_k} [M_q(k, n_{\alpha}, K)]^* M_{q'}(k, n_{\alpha}, K'), \quad (\text{B8})$$

and Δ_e is given in Eq. (33) of the main text. The quantity $2\Delta_e$ can be interpreted as an effective Stark shift [31] that is introduced by the single-photon states. Before the adiabatic elimination, energies are measured relative to the energy $2\hbar\omega_e$ of the initial state. After the adiabatic elimination, the state with two emitter excitations is “detuned with respect to itself.” The Stark shift was set to zero in Ref. [31]. This approximation is justified when the resonance wave vector lies in the middle of the band. Near the bottom of the band, however, the quantity $2\Delta_e$ introduces a nonperturbative correction [32].

The quantity $G_{K,K'}(n_1, n_2)$ describes effective off-diagonal couplings between two-photon bound states with center-of-mass wave numbers K and K' . Before the adiabatic elimination, the right-hand side of the equation for $\dot{c}_{K,b}(t)$ does not depend on $c_{K',b}(t)$ for $K' \neq K$. After the adiabatic elimination, the right-hand side of the equation for $\dot{c}_{K,b}(t)$ depends on $c_{K',b}(t)$ for $K' \neq K$.

The equations above simplify significantly if the contributions from the scattering states are dropped. The result is given in Eqs. (26)–(29) of the main text. The next step is to go to a rotating frame. Rewriting the coupled equations in terms of $\tilde{c}_{ee}(t)$ and $\tilde{c}_{K,b}(t)$, where

$$\tilde{c}_{ee}(t) = \exp(2i\Delta_e t/\hbar) c_{ee}(t) \quad (\text{B9})$$

and

$$\tilde{c}_{K,b}(t) = \exp(i\Delta_{K,b} t/\hbar) c_{K,b}(t), \quad (\text{B10})$$

the diagonal terms vanish:

$$i\hbar\dot{\tilde{c}}_{ee}(t) = \frac{g^2}{J\sqrt{N}} \sum_K F_{K,b}(n_1, n_2) \exp\left(-\frac{i\tilde{\Delta}_{K,b} t}{\hbar}\right) \tilde{c}_{K,b}(t) \quad (\text{B11})$$

and

$$i\hbar\dot{\tilde{c}}_{K,b}(t) = \frac{g^2}{J\sqrt{N}} [F_{K,b}(n_1, n_2)]^* \exp\left(\frac{i\tilde{\Delta}_{K,b} t}{\hbar}\right) \tilde{c}_{ee}(t) \quad (\text{B12})$$

with

$$\tilde{\Delta}_{K,b} = \Delta_{K,b} - 2\Delta_e. \quad (\text{B13})$$

We now specialize to the initial state $|e, e, \text{vac}\rangle$. Integrating Eq. (B12) and using the result in Eq. (B11), we obtain an equation for the coefficient $\tilde{c}_{ee}(t)$ that is independent of $\tilde{c}_{K,b}(t)$:

$$\dot{\tilde{c}}_{ee}(t) = - \int_0^t \mathcal{M}(t', n_1, n_2) \tilde{c}_{ee}(t - t') dt', \quad (\text{B14})$$

where the bath memory function $\mathcal{M}(t', n_1, n_2)$ reads

$$\mathcal{M}(t', n_1, n_2) = \frac{g^4}{\hbar^2 J^2 N} \sum_K |F_{K,b}(n_1, n_2)|^2 \exp\left(-\frac{i\tilde{\Delta}_{K,b} t'}{\hbar}\right). \quad (\text{B15})$$

Following the same steps as in Appendix A and defining the density of states $\rho(K)$ through

$$\rho(K) = J \left(\frac{\partial \Delta_{K,b}}{\partial K} \right)^{-1}, \quad (\text{B16})$$

we find Eq. (31) of the main text.

-
- [1] I. Rotter and J. P. Bird, A review of progress in the physics of open quantum systems: Theory and experiment, *Rep. Prog. Phys.* **78**, 114001 (2015).
- [2] H. Breuer and F. Petruccione, *The Theory of Open Quantum Systems* (Oxford University, New York, 2002).
- [3] G. Guarnieri, M. Kolář, and R. Filip, Steady-State Coherences by Composite System-Bath Interactions, *Phys. Rev. Lett.* **121**, 070401 (2018).
- [4] M. Schlosshauer, Decoherence, the measurement problem, and interpretations of quantum mechanics, *Rev. Mod. Phys.* **76**, 1267 (2005).
- [5] M. Schlosshauer, *Decoherence and the Quantum-to-Classical Transition* (Springer-Verlag, Berlin, 2007).
- [6] J. T. Barreiro, M. Müller, P. Schindler, D. Nigg, T. Monz, M. Chwalla, M. Hennrich, C. F. Roos, P. Zoller, and R. Blatt, An open-system quantum simulator with trapped ions, *Nature (London)* **470**, 486 (2011).
- [7] S. Diehl, E. Rico, M. A. Baranov, and P. Zoller, Topology by dissipation in atomic quantum wires, *Nat. Phys.* **7**, 971 (2011).
- [8] Y. Yanay and A. A. Clerk, Reservoir engineering with localized dissipation: Dynamics and prethermalization, *Phys. Rev. Research* **2**, 023177 (2020).
- [9] Z.-P. Cian, G. Zhu, S.-K. Chu, A. Seif, W. DeGottardi, L. Jiang, and M. Hafezi, Photon Pair Condensation by Engineered Dissipation, *Phys. Rev. Lett.* **123**, 063602 (2019).
- [10] T. Botzung, S. Diehl, and M. Müller, Engineered dissipation induced entanglement transition in quantum spin chains: From logarithmic growth to area law, *Phys. Rev. B* **104**, 184422 (2021).
- [11] P. Zapletal, A. Nunnenkamp, and M. Brunelli, Stabilization of Multimode Schrödinger Cat States Via Normal-Mode Dissipation Engineering, *PRX Quantum* **3**, 010301 (2022).
- [12] A. Tomadin, S. Diehl, and P. Zoller, Nonequilibrium phase diagram of a driven and dissipative many-body system, *Phys. Rev. A* **83**, 013611 (2011).
- [13] C. E. Bardyn, M. A. Baranov, C. V. Kraus, E. Rico, A. Imamoglu, P. Zoller, and S. Diehl, Topology by dissipation, *New J. Phys.* **15**, 085001 (2013).
- [14] M. Lemesko and H. Weimer, Dissipative binding of atoms by non-conservative forces, *Nat. Commun.* **4**, 2230 (2013).
- [15] H. Weimer, A. Kshetrimayum, and R. Orús, Simulation methods for open quantum many-body systems, *Rev. Mod. Phys.* **93**, 015008 (2021).
- [16] G. Calajó, F. Ciccarello, D. Chang, and P. Rabl, Atom-field dressed states in slow-light waveguide QED, *Phys. Rev. A* **93**, 033833 (2016).
- [17] J. Douglas, H. Habibian, C.-L. Hung, A. V. Gorshkov, H. J. Kimble, and D. E. Chang, Quantum many-body models with cold atoms coupled to photonic crystals, *Nat. Photonics* **9**, 326 (2015).
- [18] L. Henriët, Z. Ristivojevic, P. P. Orth, and K. L. Hur, Quantum dynamics of the driven and dissipative Rabi model, *Phys. Rev. A* **90**, 023820 (2014).
- [19] F. A. Wolf, M. Kollar, and D. Braak, Exact real-time dynamics of the quantum Rabi model, *Phys. Rev. A* **85**, 053817 (2012).
- [20] M.-J. Hwang, R. Puebla, and M. B. Plenio, Quantum Phase Transition and Universal Dynamics in the Rabi Model, *Phys. Rev. Lett.* **115**, 180404 (2015).
- [21] F. Altintas and R. Eryigit, Dissipative dynamics of quantum correlations in the strong-coupling regime, *Phys. Rev. A* **87**, 022124 (2013).
- [22] S. Mahmoodian, Chiral Light-Matter Interaction beyond the Rotating-Wave Approximation, *Phys. Rev. Lett.* **123**, 133603 (2019).
- [23] A. Frisk Kockum, A. Miranowicz, S. D. Liberato, S. Savasta, and F. Nori, Ultrastrong coupling between light and matter, *Nat. Rev. Phys.* **1**, 19 (2019).
- [24] P. Forn-Díaz, L. Lamata, E. Rico, J. Kono, and E. Solano, Ultrastrong coupling regimes of light-matter interaction, *Rev. Mod. Phys.* **91**, 025005 (2019).
- [25] E. Sánchez-Burillo, D. Zueco, L. Martín-Moreno, and J. J. García-Ripoll, Dynamical signatures of bound states in waveguide QED, *Phys. Rev. A* **96**, 023831 (2017).
- [26] G. Díaz-Camacho, D. Porras, and J. J. García-Ripoll, Photon-mediated qubit interactions in one-dimensional discrete and continuous models, *Phys. Rev. A* **91**, 063828 (2015).
- [27] G. Díaz-Camacho, A. Bermudez, and J. J. García-Ripoll, Dynamical polaron Ansatz: A theoretical tool for the ultrastrong-coupling regime of circuit QED, *Phys. Rev. A* **93**, 043843 (2016).
- [28] D. L. Hurst and P. Kok, Analytic few-photon scattering in waveguide QED, *Phys. Rev. A* **97**, 043850 (2018).
- [29] K. Piasotski and M. Pletyukhov, Diagrammatic approach to scattering of multiphoton states in waveguide QED, *Phys. Rev. A* **104**, 023709 (2021).
- [30] F. Dinc, Diagrammatic approach for analytical non-Markovian time evolution: Fermi's two-atom problem and causality in waveguide quantum electrodynamics, *Phys. Rev. A* **102**, 013727 (2020).
- [31] Z. Wang, T. Jaako, P. Kirton, and P. Rabl, Supercorrelated Radiance in Nonlinear Photonic Waveguides, *Phys. Rev. Lett.* **124**, 213601 (2020).
- [32] J. Talukdar and D. Blume, Undamped Rabi oscillations due to polaron-emitter hybrid states in non-linear photonic wave guide coupled to emitters (unpublished).
- [33] Note that our definition of the detuning δ differs from that employed in Ref. [31].
- [34] T. Shi, Y.-H. Wu, A. González-Tudela, and J. I. Cirac, Bound States in Boson Impurity Models, *Phys. Rev. X* **6**, 021027 (2016).

- [35] P. Lambropoulos and D. Petrosyan, *Fundamentals of Quantum Optics and Quantum Information* (Springer, New York, 2007).
- [36] R. Piil and K. Mølmer, Tunneling couplings in discrete lattices, single-particle band structure, and eigenstates of interacting atom pairs, *Phys. Rev. A* **76**, 023607 (2007).
- [37] N. Nygaard, R. Piil, and K. Mølmer, Two-channel Feshbach physics in a structured continuum, *Phys. Rev. A* **78**, 023617 (2008).
- [38] M. Valiente and D. Petrosyan, Two-particle states in the Hubbard model, *J. Phys. B* **41**, 161002 (2008).
- [39] D. Petrosyan, B. Schmidt, J. R. Anglin, and M. Fleischhauer, Quantum liquid of repulsively bound pairs of particles in a lattice, *Phys. Rev. A* **76**, 033606 (2007).
- [40] J. J. Sakurai and J. Napolitano, *Modern Quantum Mechanics*, 2nd ed. (Cambridge University, New York, 2017).
- [41] O. Firstenberg, T. Peyronel, Q.-Y. Liang, A. V. Gorshkov, M. D. Lukin, V. Vuletić, Attractive photons in a quantum nonlinear medium, *Nature (London)* **502**, 71 (2013).
- [42] K. Winkler, G. Thalhammer, F. Lang, R. Grimm, J. H. Denschlag, A. J. Daley, A. Kantian, H. P. Büchler, and P. Zoller, Repulsively bound atom pairs in an optical lattice, *Nature (London)* **441**, 853 (2006).
- [43] W. H. Press, S. A. Teukolsky, W. T. Vetterling, and B. P. Flannery, *Numerical Recipes in C The Art of Scientific Computing*, 2nd ed. (Cambridge University Press, 1986).
- [44] P. Bykov, Spontaneous emission from a medium with a band spectrum, *Sov. J. Quantum Electron.* **4**, 861 (1975).
- [45] A. G. Kofman, G. Kurizki, and B. Sherman, Spontaneous and induced atomic decay in photonic band structures, *J. Mod. Opt.* **41**, 353 (1994).
- [46] D. E. Chang, J. S. Douglas, A. González-Tudela, C.-L. Hung, and H. J. Kimble, Colloquium: Quantum matter built from nanoscopic lattices of atoms and photons, *Rev. Mod. Phys.* **90**, 031002 (2018).
- [47] S. John and J. Wang, Quantum Electrodynamics Near a Photonic Band Gap: Photon Bound States and Dressed Atoms, *Phys. Rev. Lett.* **64**, 2418 (1990).
- [48] H. J. Carmichael, *Statistical Methods in Quantum Optics 2: Non-Classical Fields*, 2008 ed. (Springer, New York, 2007).
- [49] A. Periwal, E. S. Cooper, P. Kunkel, J. F. Wienand, E. J. Davis, and M. Schleier-Smith, Programmable interactions and emergent geometry in an array of atom clouds, *Nature* **600**, 630 (2021).
- [50] F. A. An, E. J. Meier, J. Ang'ong'a, and B. Gadway, Correlated Dynamics in a Synthetic Lattice of Momentum States, *Phys. Rev. Lett.* **120**, 040407 (2018).
- [51] M. A. Perlin, D. Barberena, M. Mamaev, B. Sundar, R. J. Lewis-Swan, and A. M. Rey, Engineering infinite-range SU(n) interactions with spin-orbit-coupled fermions in an optical lattice, *Phys. Rev. A* **105**, 023326 (2022).
- [52] S. John and T. Quang, Spontaneous emission near the edge of a photonic band gap, *Phys. Rev. A* **50**, 1764 (1994).
- [53] N. M. Sundaesan, R. Lundgren, G. Zhu, A. V. Gorshkov, and A. A. Houck, Interacting Qubit-Photon Bound States with Superconducting Circuits, *Phys. Rev. X* **9**, 011021 (2019).
- [54] A. González-Tudela and J. I. Cirac, Markovian and non-Markovian dynamics of quantum emitters coupled to two-dimensional structured reservoirs, *Phys. Rev. A* **96**, 043811 (2017).